The Spatiotemporal Variability of the Internal Wave Field in the Southern Ocean

A thesis submitted in partial fulfillment of the requirements for the degree of Bachelor of Science (Advanced) (Honours)

by

Nick Velzeboer

Supervisor:
Dr. Callum J. Shakespeare

Earth Physics
Research School of Earth Sciences
The Australian National University

October 29, 2019

Australian National University

Declaration

This thesis is an account of research undertaken between January 2019 and November 2019 at The Research School of Earth Sciences, The Australian National University, Canberra, Australia.

Except where acknowledged in the customary manner, the material presented in this thesis is, to the best of my knowledge, original and has not been submitted in whole or part for a degree in any university.

Nick Velzeboer

October 29, 2019

Acknowledgements

I would like to thank my supervisor Callum Shakespeare. He has been an excellent supervisor throughout the project, and I have always enjoyed working with him. I would also like to thank Angus Gibson for his contribution to the set-up of the MITGCM model for this project. I would like to thank my partner, Emma Robertson. She has been very supportive of me during this endeavour, and made it very easy for me to work extra hard. I would also like to thank everyone in the CFP office, my parents, brothers, sister and friends for their support.

This work was completed with financial support from the ARC Centre of Excellence for Climate Extremes (CLEX) Honours Scholarship and the ANU PBSA Partnership - Spotless Scholarship. Numerical simulations and analysis were conducted on the National Computational Infrastructture (NCI) facility, Canberra, Australia.

Abstract

The spatiotemporal variability in deep ocean mixing influences the global overturning circulation, which transports, absorbs, and mixes nutrients, and heat through the ocean. It is currently an open question what the relative contributions by a variety of candidate mechanisms to deep ocean mixing are. It is widely believed that internal waves are the dominant source of deep ocean mixing. This thesis investigates the spatiotemporal variability of the internal wave field in the Scotia Sea, a region in the Southern Ocean. The Southern Ocean has strong surface winds and deep ocean flows, therefore being a prime location for the generation of wind waves, internal tides, and lee waves. The relative contributions to the kinetic energy of these different types of waves is quantified as a proxy for deep ocean mixing. To investigate the spatiotemporal variability of the internal wave field, and estimate the different contributions to deep ocean mixing, a 3D, nested, numerical ocean model is run for one year. A novel filtering technique is applied to the flow field, separating it into wave and nonwave components. In our model, we find that the M_2 internal tide has the largest kinetic energy of the different wave bands analysed at all depths in the Scotia Sea, and therefore has the most potential to contribute to deep ocean mixing. In addition, the M_2 internal tide is found to be more variable in time than expected ($\pm 15\%$). The second largest contribution to the kinetic energy in the internal wave field at all depths is made by near-inertial waves, which was found to be highly variable ($\pm 63\%$). The kinetic energy contained in the lee wave frequency band is found to be the third largest contribution to the internal wave field near the bottom of the ocean. Therefore, it likely makes a smaller contribution to deep ocean mixing than has been suggested by recent studies. In addition, our results suggest that the M_2 internal tide must be considered as a potentially important source of mixing, and current mixing parameterisations may need to be updated to take the temporal variability of the M_2 internal tide into account.

Contents

List of Figures

List of Tables

Chapter 1

Introduction

This chapter has four sections. In section 1.1, the global meridional overturning circulation will be discussed. In section 1.2, the various types of waves that are relevant for this work are briefly explained. In section 1.3, general internal wave theory will be reviewed, and then particularised for three types of waves that we consider here. Finally, in section 1.4, the aims of this thesis will be outlined.

1.1 The global meridional overturning circulation

The global meridional overturning circulation (MOC) is the large scale convective motion of the ocean. It is often referred to as the global ocean conveyor belt. Fluid parcels move up and down in different locations (overturning) and, on average, most of the motion occurs along longitudinal lines (meridional). Important movements also occur latitudinally, however. The MOC is responsible for absorbing, transporting, and mixing heat, carbon, and nutrients in the ocean, and plays a major role in the global climate system. And as we will discuss, internal waves, which are waves traveling through the interior of the ocean, are thought to be important in sustaining the MOC.

The simplest view of the overturning circulation is that dense water forms near the poles in each hemisphere, sinks to the bottom of the ocean, is subsequently horizontally transported to the equator, and then upwells. In this view, as pointed out by Munk and Wunsch (1998), one might expect the deep ocean to be filled with dense water. Only dense water near the surface ocean would be heated by surface forcing and upwell. That is, only an overturning circulation would occur in the surface ocean, and the rest of the ocean would be filled with cold, dense water. However, this assumes that isopycnals (lines or surfaces of equal density) are flat across the ocean, while in fact, isopycnals that outcrop near the poles can be found to go down to approximately 1 km (Garrett, 2001). Hence, surface forcing is indirectly applied down to approximately 1 km. From this, continuing with the above view, one might then expect that below 1 km depth, the ocean would contain unmoving cold, dense water. This is not the case, however. Deep ocean diapycnal mixing[1] allows dense water to mix upwards. Munk (1966) suggested that in order to maintain the observed stratification[2], given global dense water formation of approximately 25-30 Sverdrups (Sverdrups are 10^6 cubic metres), a deep ocean diapycnal mixing value of 10^{-4} m^2/s would be required. Globally, this would require approximately 2 TW of energy input into deep ocean mixing (Munk and Wunsch, 1998; Wunsch and Ferrari, 2004).

[1] Diapycnal refers to transfers between adjacent density layers.
[2] Stratification refers to the local vertical density gradient in a fluid column.

Multiple authors have proposed the 2TW energy for deep ocean mixing is supplied by near-inertial internal waves, generated by the wind, and internal tides (Munk and Wunsch, 1998; Garrett, 2001; Wunsch and Ferrari, 2004), although this remains an active area of research. However, as pointed out by Webb and Suginohara (2001), deep ocean mixing might only need to mix deep water around Antarctica until it reaches the density of deep water in the Southern Ocean. From there, Ekman suction brings the fluid to the surface, where it is modified by surface forcing. Ekman suction is upwelling caused by wind-driven divergence of water near the surface; that is, when water is displaced near the surface, it must be replenished. Once the fluid is near the surface, it is modified by surface forcing. Webb and Suginohara (2001) estimate this might reduce the mixing necessary to approximately 0.6 TW. In addition, Griffiths and Hughes (2004) and Hughes, Hogg, and Griffiths (2009) suggest that available potential energy is also important to the global overturning circulation, in particular, the available potential energy conversion might provide an additional 0.5 TW to the approximate 2 TW required. Taken together, given that the 2TW energy necessary is exact, this result implies that only approximately 0.1 TW would be necessary to go into mixing. There are a range of views in the literature on this subject. In any case, deep ocean diapycnal mixing is a necessary process in sustaining the global MOC.

The spatiotemporal distribution and variability of deep ocean mixing remains poorly understood, yet it is thought to have major consequences for the global climate system. Melet, Legg, and Hallberg (2016) and MacKinnon et al. (2017) suggest that both the magnitude and spatiotemporal distribution of deep ocean mixing affect ocean carbon and heat uptake, main thermocline thickness, and consequently both the regional and the global mean climate state, as well as future climate change on shorter time scales. Thus it is imperative to understand the spatiotemporal variability in deep ocean mixing, which in turn requires understanding the spatiotemporal variability in the the ocean internal wave field, which is the topic under investigation in this work.

1.2 Overview of internal waves

The spatiotemporal variability of the internal wave field depends much on the types of internal waves that are present and their relative magnitudes, which depends on a number of factors with such as the local latitude, depth, bathymetry, the time of year, the presence of storms, and strong bottom flows. Internal waves may be categorised by their generation mechanism into three types, though there are more. Here we will provide a brief overview of the different types of internal waves that will be relevant to this work, and a brief conceptual outline of internal wave propagation, before going into theory.

In short, lee waves are generated by deep ocean mean flows impinging on seafloor topography. In more detail, a bottom mean flow U_0 advects fluid parcels towards a topographic obstacle. As the fluid parcels cross the obstacle, they are forced out of their position of neutral buoyancy. The buoyancy force attempts to restore the fluid parcel to its position of neutral buoyancy but overshoots. Consequently, the fluid parcel thus continues to oscillate, radiating waves away from the lee of the hill. Lee waves have a frequency given by kU_0, where k is the wavenumber[3] associated with the topography, and U_0 the bottom mean flow. Lee waves are generated near the bottom of the ocean, and are thought to decay over approximately the first 2 km above their generation site, and thereby induce

[3] A wavenumber K is the inverse of the wavelength λ, related by $K = 2\pi/\lambda$.

Name	**Ang. freq. (rad/s)**	**Freq. (cpd)**	**Description**
ω_{lee}	kU	kU	Lee wave frequency
f_{model}	$2\pi\Omega\sin(\varphi)$	1.658	Inertial (Coriolis) frequency
M_2	1.405×10^{-4}	1.932	Semi-diurnal tidal frequency
S_2	1.454×10^{-4}	1.999	Semi-diurnal tidal frequency
O_1	6.76×10^{-5}	0.9288	Diurnal tidal frequency
K_1	7.292×10^{-5}	1.003	Diurnal tidal frequency
P_1	7.252×10^{-5}	0.9984	Diurnal tidal frequency
Q_1	6.496×10^{-5}	0.8928	Diurnal tidal frequency
N_2	1.379×10^{-4}	1.896	Semi-diurnal tidal frequency
K_2	1.458×10^{-4}	2.006	Semi-diurnal tidal frequency

Table 1.1: List of Lagrangian frequencies of different types of waves. Lee waves have a Lagrangian frequency of kU, where $k = 2\pi/\lambda_h$ is the horizontal wavenumber, λ_h is the horizontal wavelength, and U is the bottom mean flow velocity, measured approximately 200 m from the bottom. Near-inertial waves are close to, but above f. Note that f in fact varies, but the model uses a constant value of f_0. The frequencies from M_2 to K_2 are tidal constituent frequencies with which internal tides propagate. Note that there are multiple semi-diurnal and diurnal frequencies.

bottom enhanced mixing, as well as being a major energy sink of geostrophic eddies (Scott et al., 2011; Nikurashin and Ferrari, 2011; Nikurashin, Vallis, and Adcroft, 2013; Yang et al., 2018). The mechanism by which waves in general contribute to mixing is by breaking and inducing turbulence. Nikurashin and Ferrari (2011) estimate the global energy input into lee waves to be approximately 0.2 TW.

Secondly, near-inertial waves are internal waves with a frequency near the inertial frequency (Coriolis frequency), which is the frequency due to the rotation of the Earth, projected onto the local vertical axis. It is the frequency of the oscillation that attempts to restore a fluid parcel to its original position. However, unlike normal harmonic oscillators, it restores the fluid parcel not by exerting an opposite force to the direction of displacement, but by acting perpendicular to the direction of motion. Without any external forces, or changes in the Coriolis frequency, the fluid parcel would move in a circle back to its original position. The Coriolis frequency is defined by $f = 2\pi\Omega\sin(\varphi)$, where Ω is Earth's rate of rotation, and φ is the latitude. Near-inertial waves are generated by surface forcing, and surface wind stress in particular. Wind stress induces surface waves. The mixed layer has a small buoyancy frequency, and thus wind-generated near-inertial waves are not likely to be generated within it. At the bottom of the mixed layer is the thermocline, from which the buoyancy frequency increases. The surface waves cause undulations in the layers at and below the thermocline. These can be thought of as displacements of fluid parcels from their position of neutral buoyancy, similar to the lee wave generation process. As the parcels oscillate, they radiate waves. Near-inertial waves exhibit higher shear than other types of internal waves (Ferrari and Wunsch, 2009; Alford et al., 2016). The amount of energy fluxed into near-inertial waves is estimated to be 1 TW (Munk and Wunsch, 1998; Wunsch and Ferrari, 2004).

Thirdly, internal tides, or tidal waves, are internal waves generated by the gravitational potential in the Earth-Moon-Sun system with the moon supplying the main part of the energy to internal tides. The various orbital motions in this system result in what are referred to as barotropic tides, which have various diurnal (daily) and semi-diurnal (half-daily) frequencies, commonly referred to as tidal constituents. These are listed in 1.1. As the moon orbits the Earth, the barotropic tides move back and forth across bathymetry

and generate internal tides in the same way that lee waves are generated. One of the key differences between lee waves and internal tides is that internal tides have a consistent frequency set by the orbits of the moon around the Earth, and the Earth around the Sun, whereas lee waves have a frequency set by the mean bottom flow, and the wavenumbers associated with the seafloor topography. The amount of tidal energy generated in total is 3.7 TW (Egbert and Ray, 2001), which is the amount going into the barotropic tides mostly dissipated by internal tides in the deep ocean and over continental shelfs. Of this, approximately 1 TW goes into internal tides in the deep ocean (Wunsch and Ferrari, 2004).

Fourth, there are spontaneously generated waves. These waves are commonly created at sharp density gradients (Shakespeare and Hogg, 2017). These waves make the fluid dynamics of the ocean more dynamic and complicated. In a idealised model, Shakespeare and Hogg (2017) finds that 70% of the generated waves re-enter the mean flow. However, this transfer from the spontaneously generated waves back to the mean flow does not necessarily occur locally. The magnitude of spontaneous generation globally is currently not clear, but it possibly provides an important contribution to the internal wave field, and to bottom mixing. Because of the direction of propagation of spontaneously generated waves being highly vertical, the waves might make a contribution to deep ocean mixing.

In Fig. 1.1, a conceptual schematic of internal wave propagation is shown. Inertial waves are defined as internal waves that oscillate at the inertial frequency, while gravity waves are defined as internal waves that oscillate at the buoyancy frequency N. These are the outer extremes of the internal wave spectrum. The Coriolis force and the buoyancy force are the restorative forces that define internal waves. Internal waves occur at frequencies $|f| < \omega < N$. The figure was taken from Shakespeare (2019).

To illustrate the relative magnitudes of different types of internal waves, an example of a power density spectrum, which shows the kinetic energy per unit frequency, is shown in Fig. 1.2 from Brearley et al. (2013). The plot shows the observed spectra for a region with a latitude of 56° S, South-East from Patagonia in the deep ocean. It is difficult to observe a lee wave signal in a spectrum in an Eulerian frame due to lee waves being stationary. They travel with the mean flow. However, the near-inertial and tidal signals can clearly be observed and have been marked on the plot. The yellow line on the plot is the inertial frequency. In the observed region, the M_2 internal tide has a frequency close to the inertial frequency, and so it is difficult to distinguish the signals.

1.3 Internal wave theory

The Lagrangian and Eulerian frame of reference

When discussing internal waves, it is necessary to understand the difference between an Eulerian frame of reference and a Lagrangian frame of reference. An Eulerian frame of reference has fixed points in space at which various quantities are measured through time, such as the speed or the temperature, while the Lagrangian frame of reference is relative to fluid parcels, measuring the quantities not at fixed points in space, but at the fluid parcels which change their positions through time. Unless motion is uniform everywhere, it is a moving frame of reference with the distance between its coordinates changing with time.

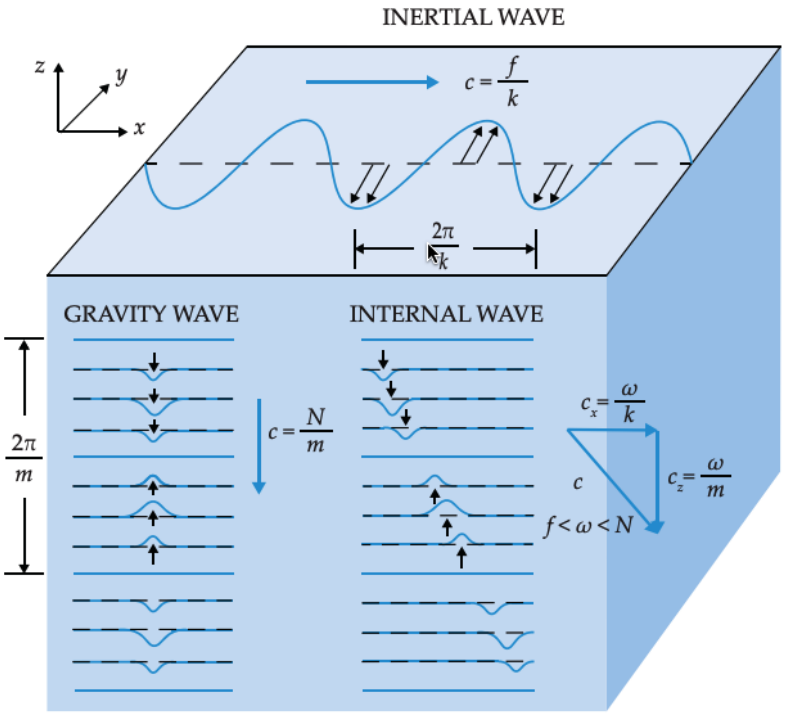

Figure 1.1: This schematic shows the physics of Internal wave propagation. Inertial waves are internal waves at the inertial frequency, while gravity waves are internal waves at the buoyancy frequency N. Internal wave have frequencies ω that satisfy $f < \omega < N$, and thus propagate both horizontally and vertically. This figure is taken from Shakespeare (2019).

Set-up of the problem

In fluid dynamics and oceanography, the central equation that describes all physics are the Navier-Stokes equations. These equations are particularised for different physical regimes. As discussed above, the Coriolis force is important to the investigation of internal waves in realistic scenarios. Hence, we begin our investigation of internal waves with the Navier-Stokes equations for a rotating fluid

$$\boldsymbol{u}_t + \boldsymbol{u} \cdot \nabla \boldsymbol{u} + f\hat{\boldsymbol{z}} \times \boldsymbol{u} = -\frac{1}{\rho}\nabla p + \boldsymbol{g} + \nu \nabla^2 \boldsymbol{u}, \tag{1.1}$$

$$\rho_t + \nabla \cdot (\rho \boldsymbol{u}) = 0, \tag{1.2}$$

where $\boldsymbol{u} = (u, v, w)$ is the velocity vector with x, y, and z velocity components, f is the inertial frequency, p is the pressure, g is gravity, ν is the kinematic viscosity, and ρ is the density. In this section, we make six assumptions.

1. The mean flow velocity only has a constant, nonzero velocity component in the x-direction U_0.
2. The fluid is inviscid ($\nu \nabla^2 \boldsymbol{u} = 0$)
3. Each of the variables can be split into a mean component and a perturbation component such that there is a balance between the mean components and a balance between the perturbation components.
4. Non-linear effects are negligible.

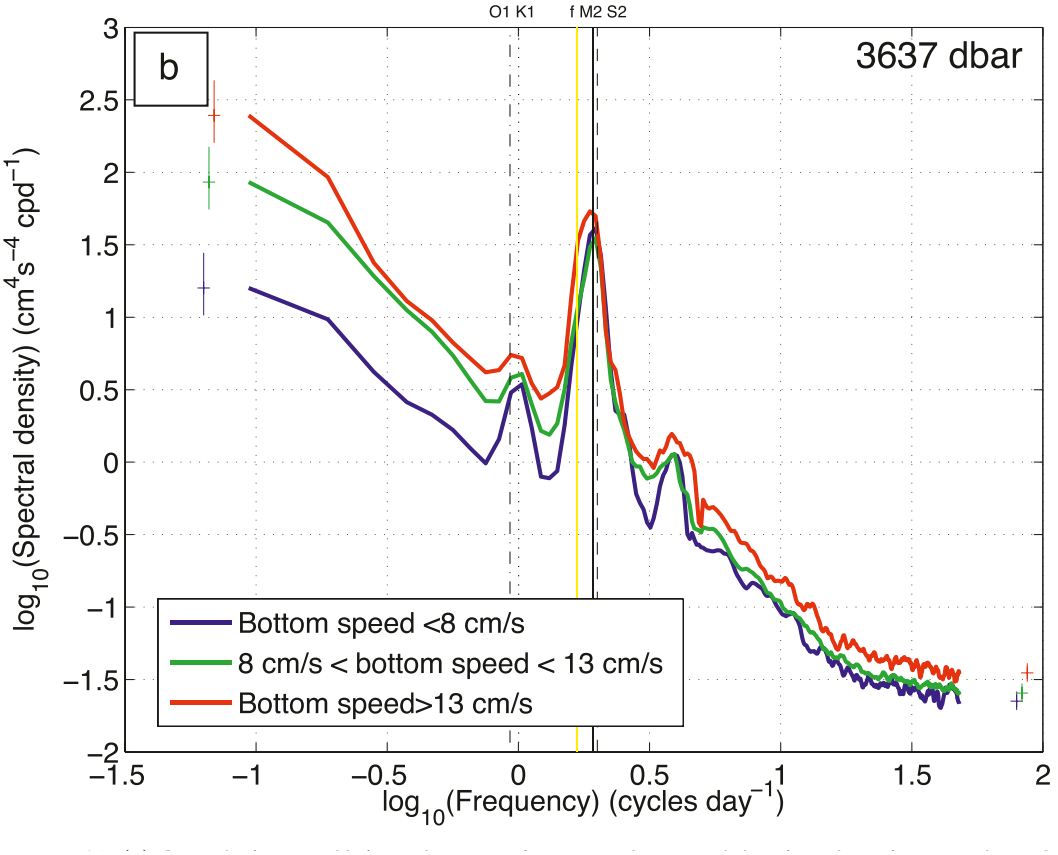

Figure 1.2: The kinetic energy spectrum taken from Brearley et al. (2013) for different bottom flow speeds. Note that this is the total kinetic energy, not the wave kinetic energy. Hence, lee waves cannot be distinguished from the background flow. However, the kinetic energy in the two diurnal and two semi-diurnal frequencies, and the Coriolis frequency can be readily observed, though it is difficult to distinguish them from one another.

5. The world is quasi-2D; that is, none of the dependent variables depends on y.
6. $\rho \approx \rho_0$ (Boussinesq approximation)

The first assumption is arbitrary. It does not matter which direction the flow is in, and it is simply convenient to pick a direction that aligns with one of our axes. The second assumption is approximately true away from the boundary layer. In addition, the effect of the viscous term is too small even at the boundary layer for it to have any significant effect on the generation and propagation of the waves. The third assumption is also arbitrary. The fourth assumption is approximately true over timescales of approximately a day. The fifth assumption is the weakest assumption. However, for waves that are simply propagating, without anything occurring along the way that interferes with their propagation, this is roughly true. The quasi-2D assumption means that we retain three dimensions of space, but without any variables being dependent on the y-dimension. The problem is essentially the same as in 3D, but shows the physics a bit clearer. Finally, the Boussinesq approximation can be made since $\rho' << \rho$. It is kept in in the gravity term, however, since there it becomes sufficiently large.

With these assumptions, we can simplify our problem. First, consider the momentum equation (1.1). Enforcing these assumptions leaves us with the following

$$\boldsymbol{u}_t + U_0 \boldsymbol{u}_x + f\hat{\boldsymbol{z}} \times \boldsymbol{u} = -\frac{1}{\rho_0}\nabla p + \boldsymbol{g}. \tag{1.3}$$

Using assumption 2, we can seperate the mean component of the balance from the perturbation component. This is also true for g. Implicitly, we have $\boldsymbol{g} = \frac{\rho_0+\rho'}{\rho}\boldsymbol{g}$. Hence, after subtracting the mean balance of the flow, we are left with the perturbation component of the equation

$$\boldsymbol{u}'_t + U_0 \boldsymbol{u}'_x + f\hat{\boldsymbol{z}} \times \boldsymbol{u}' = -\frac{1}{\rho_0}\nabla p' - \frac{\rho'}{\rho_0} g\hat{\boldsymbol{z}}. \tag{1.4}$$

In addition, from the conservation of mass equation, we can obtain the buoyancy equation and the continuity equation. Linearising, we obtain

$$\rho_t + U_0\rho'_x + \rho_0 u'_x + w'(\rho_0)_z + \rho_0 w'_z = 0. \tag{1.5}$$

In addition, note that using the vector identity $\nabla \cdot (\rho\boldsymbol{u}) = \nabla\rho \cdot \boldsymbol{u} + \rho(\nabla \cdot \boldsymbol{u})$, we find that $\rho_t + \nabla \cdot (\rho\boldsymbol{u}) = 0 \equiv \rho_t + \boldsymbol{u} \cdot \nabla\rho + \rho(\nabla \cdot \boldsymbol{u}) = 0$. Assuming incompressibility, the density for any Lagrangian fluid volume does not change with time. That is, $D\rho/Dt = 0$. Since $D\rho/Dt = \rho_t + \boldsymbol{u} \cdot \nabla\rho = \rho(\nabla \cdot \boldsymbol{u})$, we find that

$$\frac{D\rho}{Dt} = \rho(\nabla \cdot \boldsymbol{u}) \tag{1.6}$$

$$\implies \nabla \cdot \boldsymbol{u} = 0. \tag{1.7}$$

Hence, multiplying by g/ρ_0, we can reduce (1.5) to

$$b_t + U_0 b_x + w' N^2 = 0, \tag{1.8}$$

where $b \equiv -\frac{g}{\rho_0}\rho'$, and $N^2 \equiv -\frac{g}{\rho_0}\frac{\partial\rho_0}{\partial z}$, which gives us our buoyancy equation. Note that since $\rho_0 = \rho_0(z)$, this is equal to $N^2 = -\frac{g}{\rho_0}\frac{d\rho_0}{dz}$. From here onwards, we will drop the primes and assume each of the dependent variables is a perturbation quantity.

Wave propagation

From above, the final equations for our internal wave problem are

$$\boldsymbol{u}_t + U_0\boldsymbol{u}_x + f\hat{\boldsymbol{z}} \times \boldsymbol{u} = -\frac{1}{\rho_0}\nabla p + b\hat{\boldsymbol{z}}, \tag{1.9}$$

$$b_t + U_0 b_x + wN^2 = 0, \tag{1.10}$$

$$\nabla \cdot \boldsymbol{u} = 0. \tag{1.11}$$

As discussed in section 1.1, lee waves, near-inertial waves, and internal tides are generated by being lifted from their position of neutral buoyancy. Hence, for this problem, we assume a buoyancy perturbation given by $b = N^2\zeta$, where ζ is a height perturbation. By taking some derivatives of equation (1.9 to 1.11) and making some substitutions, we obtain the following

$$\Big[(\partial_x^2 + \partial_z^2)(\partial_t + U_0\partial_x)^2 - N^2\partial_x^2 - f^2\partial_z^2\Big]w = 0. \tag{1.12}$$

Since the set of operations on the LHS is a linear operator, we can assume a plane wave solution of the form

$$w = w_0 e^{-i(kx+mz+\omega t)}, \tag{1.13}$$

where k is the horizontal wavenumber, m the vertical wavenumber, and ω the Lagrangian frequency. Substituting this into Eq. 1.12, and rearranging, we find the dispersion relation

$$\omega = kU_0 \pm \sqrt{\frac{k^2N^2 + m^2f^2}{k^2 + m^2}}. \tag{1.14}$$

The first term on the RHS in the equation is referred to as a Doppler shift. The presence of a mean flow can change the effective frequency of the wave in the Eulerian frame of reference. This equation can be rearranged for the slope of wave propagation

$$\frac{m}{k} = \sqrt{\frac{N^2 - (\omega - U_0k)^2}{(\omega - U_0k)^2 - f^2}}. \tag{1.15}$$

Note that as the waves propagate upwards or downwards, N can change. Hence, their wave slope can change with height. A wave travelling from the bottom to the top will have an increasingly horizontal wave slope, while a wave traveling from the top to the bottom will have an increasingly vertical wave slope. In addition, note that it is possible to obtain a simpler expression by setting U_0 to 0 for the above equation, as well as subsequent equations, giving a simpler picture of the physics of the problem. Using the dispersion relation, we can find also find the horizontal and vertical group velocities. The horizontal group velocity $(\partial\omega/\partial dk)$ is given by

$$c_h = U_0 + \frac{(N^2 - (\omega - kU_0)^2)((\omega - kU_0)^2 - f^2)}{(N^2 - f^2)(\omega - kU_0)}. \tag{1.16}$$

Note here that the Doppler shift kU_0 can also change the horizontal velocity of the wave. Note that U_0 can be both positive and negative, so it can reduce and enhance the horizontal group speed of the wave. The vertical group velocity $(\partial\omega/\partial m)$ is given by

$$c_z = \frac{1}{k(\omega - U_0k)}\sqrt{\frac{(\omega - U_0k)^2 - f^2}{N^2 - (\omega - U_0k)^2}}.\frac{\left(N^2 - (\omega - kU_0)^2\right)\left((\omega - U_0k)^2 - f^2\right)^2}{N^2 - f^2} \tag{1.17}$$

This equation only holds true if the waves are freely propagating (without damping). That is, when

$$f^2 \leq (\omega + U_0 k)^2 \leq N^2 \quad \text{or} \quad N^2 \leq (\omega + U_0 k)^2 \leq f^2 \tag{1.18}$$

The former case is true throughout most of the ocean. However, the latter case is true in only special circumstances, such as flow being very close to the topography. This means that through some small boundary layer, the waves are damped. Since this is very small in general, this reduction in N^2 is unlikely to have much of an effect on wave propagation or generation. In the absence of a mean flow in the open ocean $U_0 = 0$, $f^2 \leq \omega^2 \leq N^2$. Without a mean flow, waves can freely propagate until they reach the critical latitude (if they do) where the inertial frequency becomes greater than their frequency. From that point onwards, the waves either reflect or become damped and dissipate quickly. However, with the presence of a mean flow, the frequency of the wave is effectively shifted and so allows propagation past the critical latitude. This shift due to the presence of a mean flow is referred to as Doppler shifting.

Lee waves

By definition, lee waves are topographically generated internal waves with zero Eulerian frequency. That is, in an Eulerian frame of reference, they are indistinguishable from the mean flow. In a Lagrangian frame, however, the waves have a frequency of kU_0. By definition, a wave must satisfy the f^2 to N^2 range, and so lee waves in a Lagrangian frame have a frequency range of $f^2 < k^2 U_0^2 < N^2$. From Eq. 1.15, the wave number ratio for a lee wave is given by

$$\frac{m}{k} = \sqrt{\frac{N^2 - U_0^2 k^2}{U_0^2 k^2 - f^2}}, \tag{1.19}$$

where ω has simply been set to zero, since it is the Lagrangian frequency. The Eulerian frequency of a general internal wave would be $\omega + U_0 k$.

Lee waves are thought to play a major role in the dissipation of mesoscale eddies, which are geostrophic[4] rotating structures of order 100 km in size. One of the outstanding problems in the literature on lee waves is the amount generated, and where they terminate. For example, in a modelling study by Nikurashin, Vallis, and Adcroft (2013), lee wave generation and bottom mixing were quantified in the Southern Ocean. They found that 80 % of lee wave energy was dissipated in the bottom ocean, which is the region from the seafloor to 2 km above. However, an observational study by Waterman, Naveira Garabato, and Polzin (2013) found that only 2-20 % of lee wave energy is dissipated in the bottom ocean. What this difference should be attributed to is still an open question, though multiple answers have been suggested.

Waterman, Naveira Garabato, and Polzin (2013) suggested three possible answers. The first answer is non-local mixing, which refers in particular to mixing in a different water column. If the mixing occurs in the same water column, it is not considered non-local mixing, even if it occurs far above the generation site. Second, it is possible that the mixing occurs higher up in the water column. That is, not within the first 2 km from the sea floor. Third, there might be non-linear effects.

[4] In oceanography, geostrophy refers to the condition of fluid flow where there is a balance between pressure and the Coriolis force.

A few other answers are possible too. One process not often considered is reflection. Wave reflection can cause waves to travel up and down the ocean multiple times before they dissipate. It possible that the generated waves dissipated outside of the region considered, which would result in a lower amount of observed dissipation, or vice versa. This fact implies that the difference found could both be smaller or larger. In addition, Shakespeare (under review) suggests that internal tides reduce lee wave generation. Taking tides into account would thus decrease the lee wave generation found in Waterman, Naveira Garabato, and Polzin (2013), and thereby increase the lee wave bottom dissipation percentage from the 2-20% to some higher range.

Internal tides

Petterson (1908) is often considered to be the first to have identified internal tides. As reviewed in Garrett and Kunze (2007), early observations by (Nansen, 1902) motivated two-layer stratified[5] fluid experiments (Zeilon, 1912) that led to an understanding of the significance of interfacial waves[6]. Internal tides are interfacial waves generated by the tides near bottom topography. Many observations and experiments have since investigated the dynamics of internal tides in the ocean. Early theory of internal tides is often considered to have been developed by Cox and Sandstrom (1962). Baines (1973) considered the generation of internal tides by surface tides interacting with bottom topography in the acoustic limit. In the acoustic limit, the horizontal excursion distance of fluid parcels advected by the background covers only some fraction of the width of an obstacle. Only Mork (1968) had considered the general problem of internal wave generation by a simple harmonic flow moving back and forth across topography in a stratified fluid. His results, however, were only valid for conditions in which the horizontal scales of the flow were much larger than the vertical scales. Bell (1975a) and Bell (1975b) considered the general problem of internal wave generation in the limit where the ocean is semi-infinite so that any effects on the generation due to propagation, such as reflection, could be ignored.

By definition, tides are internal waves of tidal frequency, as listed in Table 1.1. Hence, from Eq. 1.14, the slope of these waves is simply given by

$$\frac{m}{k} = \sqrt{\frac{N^2 - (\omega_t + U_0 k)^2}{(\omega_t + U_0 k)^2 - f^2}}. \tag{1.20}$$

Generally, internal tides have strong signals at each of their harmonics. This is because the fundamental frequency is sensitive to the slope of the obstacle, the first harmonic is sensitive to the gradient in the slope, the second harmonic in the gradient of the gradient of the slope, and so forth Bell, 1975a. Without Doppler shifting, tides generate two beams on both side of the topographic obstacle. However, with Doppler shifting, asymmetric generation occurs. If the Doppler shifting is sufficiently strong, pushing one of the propagation slopes to below horizontal, one of the beams is not generated at all.

Near-inertial waves

Early theoretical work on near-inertial waves was done by Fu (1981). Based on then recent experiments, he examined the spectral peak that occurred near the inertial frequency and

[5] Stratification of fluids refers to the structure of density layers and the spatial gradients between them.
[6] Interfacial waves simply refers to waves propagating along the interface of two different density layers.

remarked that it could either be due to local forcing or due to remote forcing. Focusing on the remote forcing, he developed a turning-point theory that agreed quite well with observations. Further theory was developed by Gill (1984) on ocean's response to storms. He identified two stages. In the short first stage, while storms are still present, surface currents are generated. In the second stage, once the storm has passed, the ocean undergoes Rossby readjustment. During Rossby readjustment, the ocean returns to equilibrium by generating near-inertial waves. and Garrett (2001), and important observations were gathered by D'Asaro et al. (1995), D'Asaro (1995a), and D'Asaro (1995b). These indicated that locally generated near-inertial waves are significant. In fact, generally, near-inertial waves are seen as predominantly wind-generated. However, near-inertial waves are generated by other mechanisms too. These include wave-wave interactions, lee waves, and geostrophic adjustment, and it is not clear what the relative contributions are by each (Alford et al., 2016).

In the open ocean, near-inertial waves, like all internal waves, obey the dispersion relation shown in Eq. 1.14, and their wave slope by Eq. 1.15 For near-inertial waves, $\omega \approx f$, which implies in general that $\omega^2 << N^2$. Hence, the wave slope gives $k/m \approx N/(\omega^2 - f^2)$. Near-inertial waves thus have a more horizontal wave slope due to their frequency ω being close to the inertial frequency. For normal values of N (order 10^{-5}), and f (order 10^{-4}), $k/m << 1$. Ignoring any Doppler shifting, the dispersion relation can then be simplified to $\omega \approx \sqrt{(f^2 + k^2)/(m^2 N^2)}$. The vertical group velocity $\partial\omega/\partial m$ is then

$$c_z \approx \frac{k^2 N^2}{f m^3} = \frac{(\omega^2 - f^2)^3}{kNf}. \tag{1.21}$$

Near the surface, the wind stress is balanced by the Coriolis force. That is, the governing equation is

$$\boldsymbol{u_t} - f\nabla(v, u, 0) = -\frac{1}{\rho_0}\nabla\boldsymbol{\tau}. \tag{1.22}$$

(Alford et al., 2016). A resonant frequency here is approximately at f, since it naturally oscillates at f. For a detailed analysis of resonance near the inertial frequency, see Whitt and Thomas (2015). Hence, when wind stress inputs energy near the surface at a host of frequencies, most of the energy will be transmitted near the inertial frequency. The total energy flux is given by $F = Ec_z$, where F is the total flux $(F_+ + F_-)$, where F_+ is the upwards and F_- is the downwards flux, E is the sum of the kinetic and potential energy, and c_z is the vertical group speed. The spectral peak does not occur at f though since the energy input might peak at f, the vertical group speed increases with frequency. Since the flux is the kinetic energy times the group speed, the spectral peak occurs slightly to the right of the inertial frequency. Finally, the spectral is also determined by the relative contributions by locally generated waves and remotely generated waves.

1.4 Aim

The aim of this thesis is to characterise the spatiotemporal variability of internal waves with a view to deep ocean mixing, and the types of internal waves that are relevant in the Scotia Sea in the Southern Ocean by running a 3D model in MITgcm. We will use a novel filtering technique referred to as Lagrangian filtering, which will enable us to clearly distinguish waves from the background flow. The results will be compared to current observations. Due to unprecedented insight into the internal wave field in the

Scotia Sea, we can reinterpret some of the observations based on our results. Finally, by running a model for one year, we will be able to discuss the seasonality of various internal wave signals, as well as events, which allows for understanding the temporal variability of observational results.

In Chapter 2, the method set-up, the topographic dataset, and the Lagrangian filtering method will be described in detail. In Chapter 3, the results will be shown, interpreted, and briefly discussed. In Chapter 4, the most salient findings from our model will be discussed with a focus on the temporal variation of the internal wave field. Finally, in Chapter 5, we will summarise the results, discuss the implications of the results, consider the caveats and limitations of this work, and outline directions for future work.

Methods

Chapter 2 has three sections. In section 2.1, we will describe the model set-up, including the physical regimes that were investigated. In section 2.2, we will discuss the seafloor topography used in the model and a modification of the topography based on newly available data. Finally, in section 2.3, we will describe the main analysis technique used to examine model output.

2.1 Model set-up

We use the Massachusetts Institute of Technology general circulation model (MITgcm) to simulate the primitive equations in an f-plane for one year. In order to allow eddies to form, and to able to track fluid parcels for more than one week, we used a large low-resolution domain. As shown in Fig. 2.1, the domain ranges from $-60°$ to $-52°$ in longitude and from $-75°$ to $-40°$ in latitude with a 150 $\times$ 150 km high resolution region centred on a region in which high-resolution, multi-beam soundings were recently taken (Jesse Cusack, pers. com.) The model has a horizontal resolution of 700 m in the high resolution domain, which tapers to 3.5 km in the larger domain. The whole domain has 200 depth levels with depth resolution ranging from 7 m to 32 m. The model uses Smagorinsky viscosity horizontally, which calculates the local dissipation based on the divergence in u and v, and a constant vertical viscosity (see Table 2.1). It has an implicit free surface, a no-slip bottom boundary, and open side boundaries.

The model is run with three configurations in order to understand the underlying physics of each regime:

1. Boundary forced (B)
2. Boundary and surface forced (S)
3. Boundary, surface, and tidally forced (T)

For configuration B, daily-updated sponges force temperature, salinity, and horizontal velocities at the side boundaries with data from the *GLORYS12V1 product* (2017). Configuration S has the same boundary forcing, and is forced at the surface using surface wind velocity, precipitation, evaporation, potential temperature, net short wave radiation, net long wave radiation and sensible heat flux fields from *ERA5 Reanalysis* (2017) data, which are hourly. Configuration C has the same boundary and surface forcing, and is tidally forced by a tidal potential over the 3D domain using TPOX8_atlas_30c data from the Tidal Model Driver (TMD) (Egbert and Erofeeva, 2002).

Parameter	**Value**	**Description**
bottomDragQuadratic	10^{-3}	Quadratic bottom drag coefficient (1)
f0	1.206×10^{-4}	Reference Coriolis parameter (1/s)
viscAz	10^{-5}	Vertical eddy viscosity coefficient (m^2/s)
viscC2smag	5	Smagorinksy harmonic viscosity parameter (non-dim)
no_slip_sides	F	Viscous boundary conditions: no-slip sides
no_slip_bottom	T	Viscous boundary conditions: no-slip bottom
diffKhT	0.1	Laplacian diffusion of heat laterally (m^2/s)
diffKzT	10^{-5}	Laplacian diffusion of heat vertically (m^2/s)
diffKhS	0.1	Laplacian diffusion of salt laterally (m^2/s)
diffKzS	10^{-5}	Laplacian diffusion of salt vertically (m^2/s)

Table 2.1: Model parameters (applied to all configurations).

2.2 The seafloor topography

To generate the topography, the GEBCO 2014 SID Grid, version 20150318 was used (www.gebco.net). In Fig. 2.1a the larger domain topography is plotted. The rectangle in the centre of the domain is a high-resolution region, which has a horizontal resolution of 30 arc seconds, and is plotted in Fig 2.1b. In the North-West, Southern tip of South-America is displayed in black, and in the North, the Falkland Islands. The yellow-saturated region is the continental shelf surrounding South-America. Significant mid=ocean ridges are present in the centre and the North-East of the domain.

The wavenumbers associated with lee wave generation are a function of the gradients in the topography, and thus it is important that the topography of the model closely matches the real topography. Comparing the GEBCO topography to a higher resolution topographic data set obtained from multi-beam soundings (Jesse Cusack, pers. com.), we found that there was a significant difference in the local topography. In Fig 2.1c, GEBCO topography is plotted for the region inside the rectangle in Fig 2.1b, and the high-resolution multi-beam soundings are displayed on the right. Note here that the topography is shown as it is in the model, for which it had to be interpolated to the 700 m horizontal grid. In the GEBCO data, the absolute maximum in height is found in the North-Eastern part of the feature, while in the multi-beam soundings, the maximum is found in the Southern part. In addition, the GEBCO data has two peaks, while the multi-beam soundings disclosed a single peak. These differences would likely result in a different wave field, such as a different spatial distribution of wave generation and propagation.

To address this problem, the higher resolution bathymetry was integrated with the GEBCO topography in the centre of the domain. To smoothly integrate it, a region was cut out of the multi-beam soundings data set, placed inside the GEBCO data, and tapered near the boundaries. The boundaries of the region ran along relatively flat topography to ensure no artificial mounts were created in the process, which are a potential source of error. The North-Western region of the domain contains the Southern end of Patagonia, which contains many small-scale channels. These caused numerical instability in the model, and were therefore masked as land in the model.

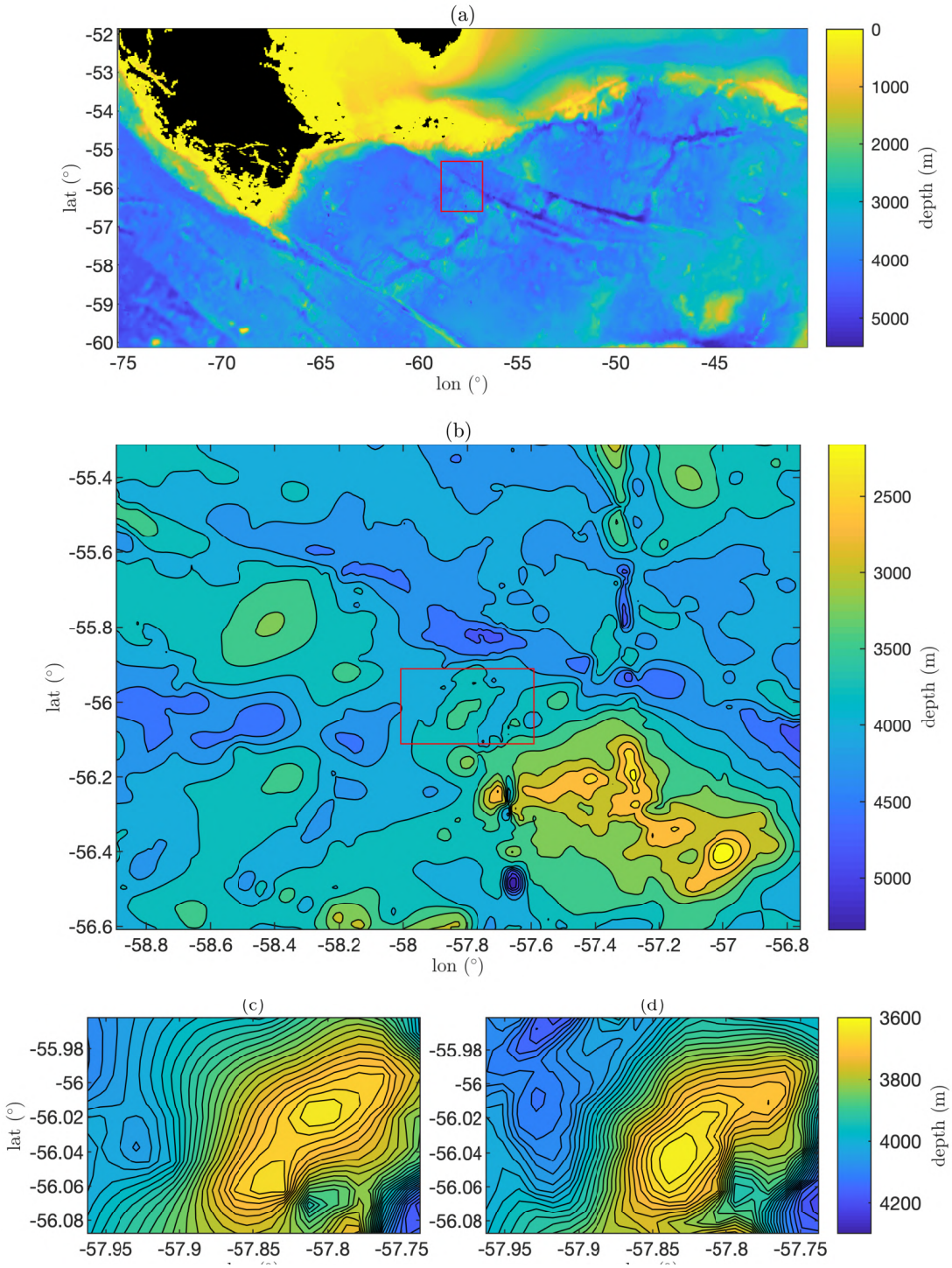

Figure 2.1: The seafloor topography used in the model are shown. The full domain topography is shown in (a), where the black region indicates land. A contour map of the region inside the red rectangle in (a) is shown in (b). This plot shows the main analysis region referred to as the domain of interest. Contour maps of the region inside the red rectangle in (b) are shown in (c) and (d). (c) displays the GEBCO topographic data set, whereas (d) is based on recent multi-beam soundings (Jesse Cusack, pers. com.). (d) has been integrated with the GEBCO topography for use in the model.

2.3 The Lagrangian filtering method

The Lagrangian filtering method has has previously been used by Nagai et al. (2015) and Shakespeare and Hogg (2017), and is outlined in section 2.3 below. It combines the idea of the Lagrangian frame of reference with the idea of a Fourier filter. In fluid dynamics and oceanography, the purpose of such a filter is to track waves relative to the mean flow, and thereby separate the wave from the nonwave components of the flow. This is made possible by the fact that waves have a minimum frequency in a Lagrangian frame of reference. Below the inertial frequency, waves become damped, and dissipate quickly. However, in a Eulerian frame of reference, waves do not have a minimum frequency due to Doppler shifting and relative vorticity. Doppler shifting occurs as a consequence of the presence of a mean flow, and shifts the frequency of the wave in a Eulerian reference frame. Lagrangian filtering is thus particularly important for identifying lee waves, since they are stationary. That is, in a Eulerian reference frame, they are difficult to distinguish from the mean flow because they have the same frequency. However, Lagrangian filtering is beneficial for all types of waves by providing a clear distintion between the wave field and the nonwave field.

The full domain algorithm

In general outlines, the algorithm is as follows:

1. Distribute parcels throughout the full domain at the start and end time
2. Advect this initial parcel distribution forwards in time
3. Seed parcel distributions at regular time intervals and backward advect them (for better concentration of parcels)
4. Fourier transform the associated quantities (u, v, w, p, ρ) of the resultant parcel paths
5. Set the signal below some scaling factor s (e.g. $s = 0.9$) times the inertial frequency f equal to 0
6. Inverse Fourier transform the same quantities to obtain the wave paths
7. Interpolate the wave paths back to the Eulerian X-Y grid

By removing the nonwave component of the flow, which is defined as having frequency below the inertial frequency, the result is the wave component. Note that part of the nonwave component (the band-pass filter being $0.9f$) is not filtered to account for the numerical resolution in frequency space and partly to account for relative vorticity causing waves to be generated slightly below the inertial frequency.

In more detail, first, in order to ensure all regions of the domain are well-resolved, one option is to distribute parcels based on the regional divergence of the horizontal velocities u and v. Without using a divergence-based distribution, these regions might have a low parcel concentration with time due to parcel advection. Another option is to distribute parcels at regular time intervals. The initial distribution is simply advected forward in time, while distributions seeded at regular time intervals after that are advected both backward and forward in time. The purpose of seeding at multiple times is increasing

parcel concentration and thereby better resolving the flow in regions that would otherwise have low parcel concentrations.

Second, the parcels are advected using a second-order Runge-Kutta method, which is a numerical scheme for solving ordinary differential equations in time, such as initial-value problems. As the parcels are advected, their locations, as well as the quantities of interest (e.g. u, v, w, p, ρ), are stored. After Fourier transforming these quantities in time, a high-pass filter is applied which sets the signal below $0.9f$ (where f is the inertial frequency, or synonymously, Coriolis frequency) equal to 0. Taking the inverse Fourier transform results in the Lagrangian wave paths in the time domain. That is, a three-dimensional array of the quantities of interest together with X and Y-locations of each particular fluid parcel through time. Using the X and Y-locations, the quantities can be interpolated from the Lagrangian field to the original X-Y grid. This final step results in a two-dimensional grid of the wave components of each of the variables of interest.

The continuous seeding algorithm

For the filtering of the model data in this project, I modified the full domain algorithm described above to obtain higher accuracy parcel paths. Instead of seeding a uniform distribution of parcels at the beginning and then at regular time intervals, it seeds a uniform distribution over the domain of interest at every time step. In short, the method is as follows:

1. Distribute parcels uniformly over the X-Y grid in the domain of interest
2. Advect the parcels forwards in time (by 84 hours)
3. Advect the parcels backwards in time (by 84 hours)
4. Fourier transform the associated quantities (u, v, w, p, ρ) of the resultant parcel paths
5. Set the signal below $0.9f$ (the inertial frequency) equal to 0
6. Inverse Fourier transform the same quantities at the original X-Y grid (made possible by starting the parcels on the X-Y grid)
7. Repeat this every time step

One difference between the two algorithms is the number of parcels required. This is due to different approaches. The full domain algorithm obtains the Lagrangian paths, and then interpolates these to the X-Y Eulerian grid, while the continuous seeding algorithm only obtains the Lagrangian paths that exactly intersect each grid point in the domain of interest. With the approach of the full domain algorithm, there is no prior knowledge of where the parcels go, and therefore, they are distributed over the full domain. The continuous seeding algorithm, however, does have prior knowledge, since it seeds the parcels at every time step exactly on every grid point in the domain of interest, and therefore requires less parcels.

In order to achieve this, however, it requires seeding at every time step. This has at least two benefits and one drawback. One consequence is that it does not require interpolation, which has the dual benefit of increasing computational efficiency and accuracy. The former is true because less parcels are required, and the latter is true because it has resolution equal to the grid scale by having a parcel at every grid point in the domain of

interest. The drawback is that seeding at every time step increases the number of times forward and backward advection needs to be completed, thereby reducing computational efficiency.

The net difference in efficiency for this model is that the continuous seeding algorithm requires approximately twice the computational time compared to the full domain algorithm. However, the improved accuracy can be important, since low parcel concentrations can lead to a number of problems. One important problem is poor interpolation, which can result in missing important features in the wave field, and sometimes even artificial generation of waves.

Results

3.1 Global overview

The model configurations and depth levels for analysis are laid out in Table 3.1. As stated in section 2, there are three forcing regimes. Run B is boundary forced, run S is boundary and surface forced, and run T is boundary, surface, and tidally forced, where the tidal forcing acts at all depths throughout the domain. The forcing regimes are mostly analysed at three depth levels (horizontal cross sections), which are at 100 m, 1400 m, and 3200 m depth. The topographic cross-sections at each of these depth levels for the subdomain are displayed in Fig. 3.1. Hence, there are 9 different cases, referred to by their forcing regime (or run) and their depth level, such as B100 or T3200, for example, as laid out in Table 3.1. Note that for all runs, the continuous seeding algorithm of the Lagrangian filtering method described in section 2.3 was used to obtain the wave component of each variable, unless specified otherwise. In addition, recall that the Lagrangian filtering method outputs the variables in the time domain. For the wavenumber and frequency parts of the results, a Fourier transform of that signal was taken to obtain the properties of the waves in the Eulerian frame of reference.

The three forcing regimes were chosen to cumulatively add different types of waves, and analyse the effects of each. Run B is boundary forced, and thus generates flow across the domain, including a mean bottom flow. The mean bottom flow generates lee waves. In addition, spontaneous wave generation is possible by sharp density fronts, though these occur less than in run S, since the surface forcing in run S generates larger density gradients than without surface forcing. The boundary forcing also induces small amplitude near-inertial waves, which contribute negligibly to the total kinetic energy. Run S allows for the generation of strong near-inertial waves since it is surface forced, and in particular, wind forced. Finally, run T allows for the generation of barotropic and internal tides. The total and wave kinetic energy for each of these runs is shown in Fig. 3.2 at each depth

	Boundary forced	Surface forced	Tidally forced
100 m	B100	S100	T100
1400 m	B1400	S1400	T1400
3200 m	B3200	S3200	T3200

Table 3.1: The forcing regimes and depth levels, and what they will be referred to. Note that the forcings accumulate from left to right. That is, run B is boundary forced, run S is boundary and surface forced, and T is boundary, surface, and tidally forced.

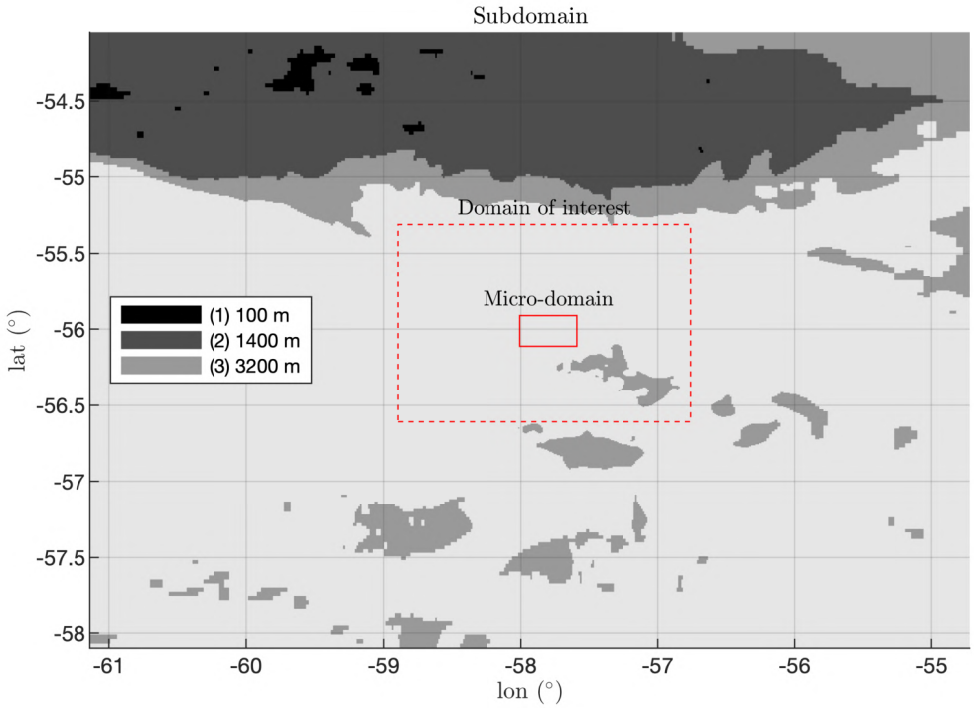

Figure 3.1: The topographic cross-sections at each depth level for different analysis regions, referred to as the subdomain, the domain of interest, and the micro-domain.

level. Note that for the tides, the barotropic component has been filtered.

The motivation for the choice of these specific depth levels is the measurement of the generation and dissipation of the waves. The first depth level at 100 m is approximately at the thermocline, which separates the mixed ocean layer from the deep ocean. It is close to the location of near-inertial wave generation and surface spontaneous wave generation. It might seem preferable to take a cross-section at a higher depth level, however, it becomes increasingly difficult to distinguish waves from background noise. The third depth level at 3200 m is only hundreds of meters removed from most of the bottom topography in the domain of interest, and thus is near the generation site of lee waves and internal tides. It also contains a cross-section of local topography, as can be seen in Fig. 3.1. The second depth level at 1400 m was chosen in order to measure what happens in between the other two depth levels. It is close to the middle, and is free from topographic cross-sections in the domain of interest. The different sizes of subdomains and their terms of reference are shown in Fig. 3.1.

The model domain is in the Scotia Sea in the Southern Ocean. Hence, the Antarctic Circumpolar Current (ACC) is present, which is a current that flows clockwise around Antarctica. The ACC is known to have high flow speeds. In the model runs, the mean surface flow speed was generally varied around 1 m/s. The kinetic energy associated with the ACC can be seen in Fig. 3.2. In addition, winds are also strong over the Southern Ocean, therefore generating a strong near-inertial wave field, as will be seen in the next section.

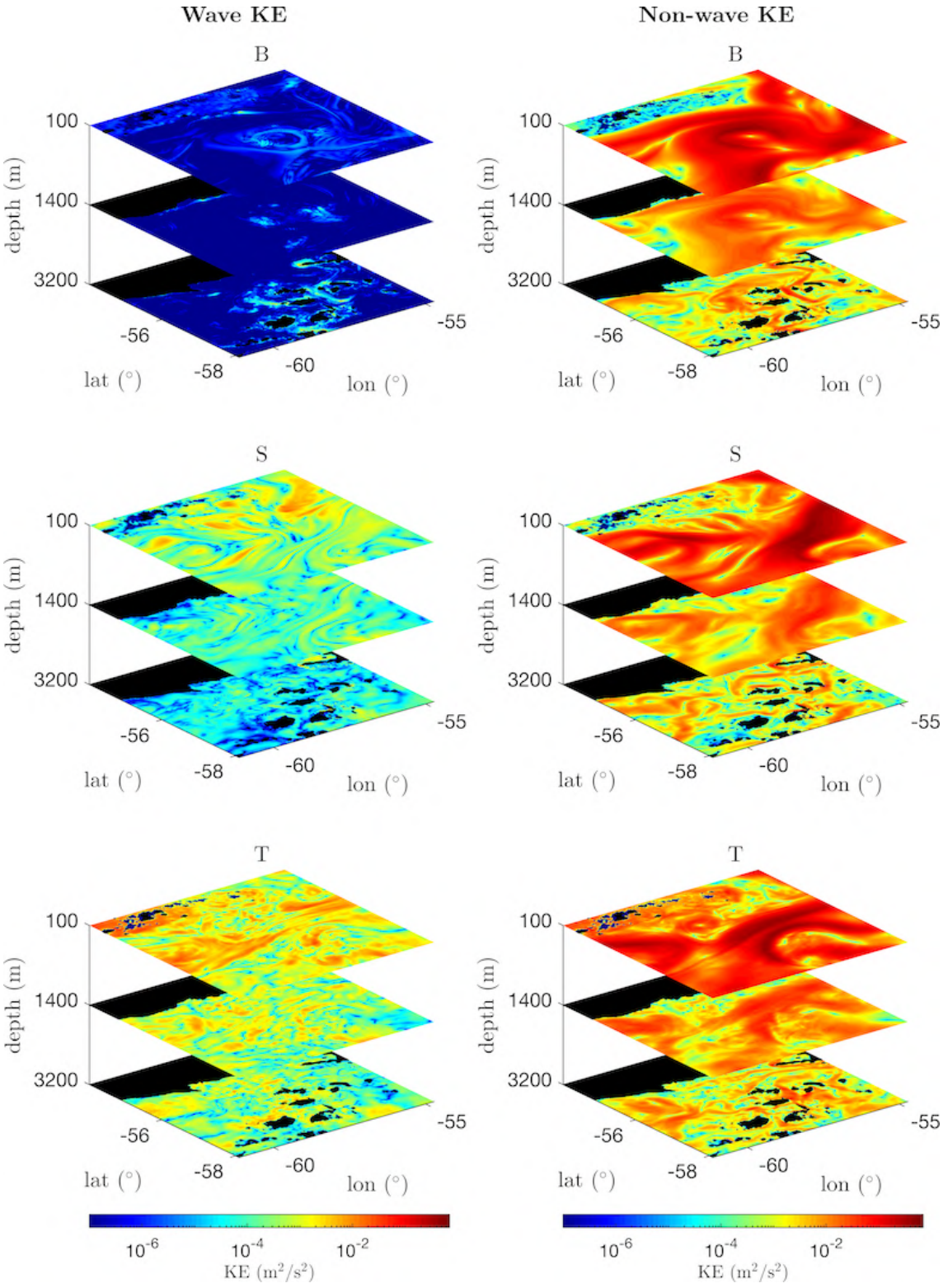

Figure 3.2: Wave kinetic energy and non-wave kinetic energy for forcing regimes B, S, and T at thee three depth levels for analysis in the subdomain. The black regions are cross-sections of the local topography. The model time of the snapshot is after 20 weeks (24 April 2010), at 12:30 PM.

3.2 Spatial variability

In Fig. 3.2, the wave kinetic energy for all runs and depth levels are plotted. On the left is the wave kinetic energy. On the right is the non-wave kinetic energy. Due to the magnitude of each, and the logarithmic plotting, the non-wave kinetic energy is indistinguishable from total kinetic energy. The first thing that becomes clear is the increase in wave kinetic energy as more forcings are introduced. Run B has the least wave kinetic energy, while run T has the most. In addition, each of the individual forcings, from boundary forcing to tidal forcing, increases in its kinetic energy contribution to the internal wave field. Tides generate the most wave kinetic energy by far, as will be seen in the next section. Clearly, it is not only the magnitude of the kinetic energy that changes. As more forcings are introduced, both the internal wave field's structure as well as total flow field's structure are altered. The spatial variability is mainly controlled by the presence of topography. The surface wind stress is a large factor as well, but is difficult to observe both due to the high level of noise in the wind stress, the low spatial resolution available, and the fact that near-inertial waves travel almost entirely horizontally with a variable wave slope.

In run B, an eddy (a large-scale rotating structure ranging from tens to hundreds of km in size) of approximately 100 km in size is present in the centre of the domain. Near the surface, this is where most of the kinetic is present. Note that due to the presence of islands in the North (the region from the left to the top corner of the domain as presented in the figure) the ACC is obstructed, and therefore the non-wave flow has little kinetic energy. In the depth level below, at 1400 m, the eddy is still present. However, the transfer to the internal wave field is negligible. The strongest signal here is lee waves generated at the bottom of the ocean, as can be seen in the depth level below, at 3200 m. At this level, the coherent eddy observed above is still present, but constrained by the topography. Many meandering streams can be observed, shaped by the seafloor topography. Strong lee wave generation occurs near topographic obstacles, both those observable in the figure, and those below the cross-section. The closer to the obstacle, the greater the wave kinetic energy. A likely explanation for the wave kinetic energy being focused in the location of the eddy is flow trapping by the eddy's relative vorticity (Kunze, 1985). Waves mostly reflect when they encounter a region where the effective inertial frequency is higher than their frequency. The eddy's relative vorticity increases the effective inertial frequency. Hence, as the waves propagate upward, and the relative vorticity increases, particularly away from the centre of the eddy, the waves are constrained to propagate within the bounds set by the eddy.

In run S, the surface forcing has complicated the non-wave flow. B coherent eddy is not present here. Note, however, that this is not necessarily typical. The time of the snapshot is the same as above for the purpose of comparison. In the internal wave field, we find a strong presence of near-inertial waves, many recognisable as wind waves. Wind waves are long in one direction, and short in the perpendicular direction. These waves propagate mostly horizontally. Hence, at the lower depth levels, most of the near-inertial waves present would be from outside the domain of interest. However, in the South-East, it seems that we can some correspondence in the internal wave field between the 100 m depth level, and the 1400 m depth level. This is likely an example of the near-inertial chimney, which is a mechanism by which eddies trap near-inertial waves with their large relative vorticity, and propagate them downward. The non-wave flow structure at 1400 m is largely the same as that of 100 m. At the bottom depth level, however, the wave and the non-wave flow have changed significantly. The non-wave flow appears similar to the non-wave flow in run B at the bottom depth level. There are many separate streams. In

the internal wave field, the near-inertial waves are clearly still present, as can be inferred from comparison with the bottom level of B. However, the long-short horizontal structure that typified near-inertial waves higher up is no longer apparent here. In addition, though obscured by the relatively strong near-inertial wave kinetic energy, we can see the presence of lee waves, particularly near the topography.

In run T, the non-wave flow does have an eddy in the South-Eastern corner, as well as a particularly coherent smaller one near the centre. Both leave a small, but noticeable mark on the internal wave field. The internal wave field looks different again to the forcing regime that came before it. This is due to the presence of both barotropic and internal tides. For example, in the Northern region, unlike B and S, topographic obstacles near the surface become a generation site for the internal wave field due to the presence of the tides. And compared to S, the internal wave field contains more small-scale waves. However, at the surface, we can still clearly see the strong presence of near-inertial waves. Note that due to fact the barotropic tide was not filtered out during the Lagrangian filtering stage, the kinetic energy in the wave field is stronger than it would be otherwise. As will be discussed later, with the barotropic tides filtered, the near-inertial waves dominate the kinetic energy near the surface. At the 1400 m depth level, we can still see the presence of the larger eddy in both the mean and wave kinetic energy. The lengths of the near-inertial waves are shorter than they were in S. At the bottom depth level, the non-wave flow looks similar to B and S. The internal wave field, however, now has a strong internal tide signal, generated by the seafloor topography.

The kinetic energy in the wavenumber-frequency space is shown in Fig. 3.3. Recall that B100 refers to the 100 m depth level of the boundary forced run, S1400 to the boundary and surface forced run at 1400 m depth, and T3200 to the boundary, surface, and tidally forced run at 3200 m. The scale of the domain of interest allowed for horizontal wavenumbers k to be observed down to the scale of 10^{-4} m^{-1}, where $k = 2\pi/\lambda_h$ and λ_h is the horizontal wavelength of a wave.

First, consider run B in Fig. 3.3. In the Eulerian frame, lee waves are close to zero frequency, and can be observed on the left of Fig. 3.3. They have a large wavenumber range, going from 10^{-4} m^{-1} to $3{\times}10^{-3}$ m^{-1}. They peak in wavenumber around $3{\times}10^{-3}$ m^{-1}, which corresponds to a 6 km wavelength, approximately. As they move closer to the surface, however, the lower wavenumber lee waves decay less than those of higher wavenumber. This is as expected, due to shorter wavelength internal waves experiencing higher shear stress, and therefore are more prone to breaking. This is accounted for in the model by using a Smagorinsky model viscosity, which scales with the divergence of the velocity field. We can also observe a small band near the inertial frequency, which is strongest from 0 to the the lowest wavenumber we can resolve of 10^{-4} m^{-1}/s.

Second, consider run S in Fig. 3.3. The lee wave signal is present for run S too, though it is reduced. The wavenumber containing the most kinetic energy is also the lowest band here, though it generates waves at higher wavenumbers too. This is not unexpected, since near-inertial waves generally have the highest kinetic energy in low wavenumbers.

Third, consider run T in Fig. 3.3. The internal tides (the barotropic tides have been filtered out here), also all generate waves over a large range, but again the most kinetic energy is contained the lowest band from 0 to 10^{-4}. The frequencies of these waves will now be considered in more detail.

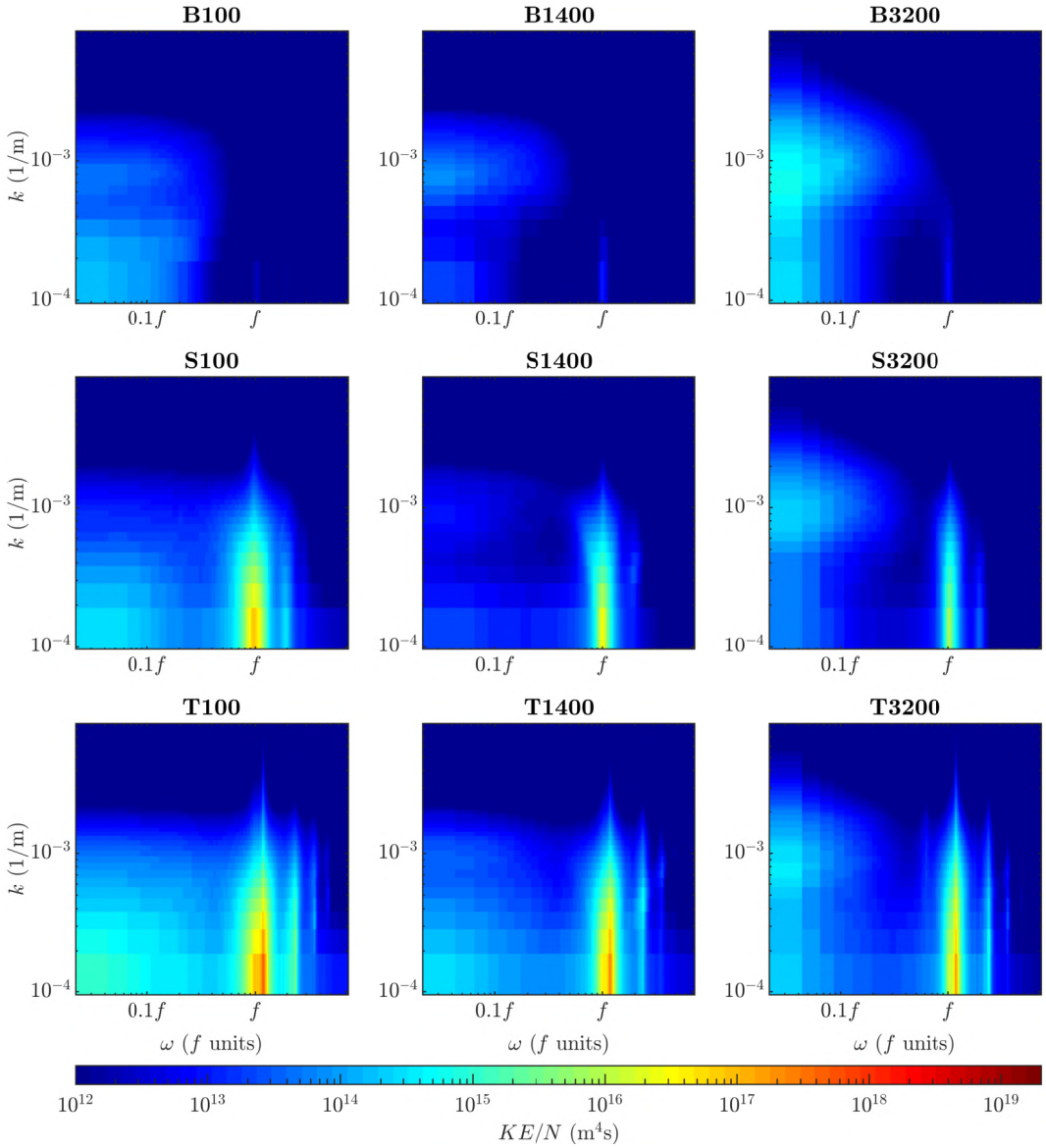

Figure 3.3: Wave kinetic energy for as a function of wavenumber and frequency for runs B, S, and T at three depth levels in the domain of interest.

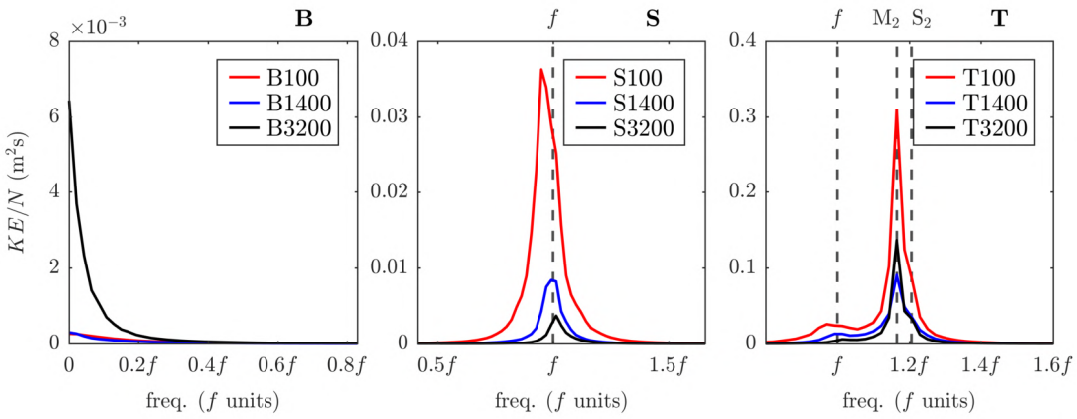

Figure 3.4: The N-scaled kinetic energy spectral density plots for the boundary forced regime (B), the surface forced regime (S), and the tidally forced regime (T) at three different depth levels at the 100 m, 1400 m, 3200 m depth levels. Plot S and T have vertical lines plotted across them, indicating the inertial frequency f, the M_2 tidal frequency, and the S_2 tidal frequency.

3.3 Kinetic energy by frequency band

In this section, we will examine the different types of waves and their associated kinetic energy. As can be seen directly from Eq. 1.15, upward wave propagatation results in the wave slope becoming increasingly horizontal due to the Brunt-Vaisala frequency N increasing with height. To correct for this effect, and thereby allow comparison of the kinetic energy at the different depth levels, we divide it by the Brunt-Vaisala frequency N. When comparing the N-scaled kinetic energy at the different depth levels, we can gauge the dissipation of the waves. To see why, note that the energy flux is given by$E_{flux} = c_z E$, where $E = KE + PE$, KE is kinetic energy, PE is potential energy, E_{flux} is the energy flux, and c_z is the vertical group speed. The energy flux is the energy the waves transport from their generation site, while the wave kinetic energy is the kinetic energy associated with the group speed of the wave (mostly the horizontal group speed, since vertical propagation is generally much smaller than horizontal propagation). The vertical group speed scales by $1/N$. Hence, by dividing the kinetic energy by N, we obtain a measure that scales roughly with the energy flux.

The yearly average N-scaled kinetic energy spectral density is plotted for run B, S, and T (see Table 3.1) at the 100 m, 1400m, and 3200 m depth levels in Fig. 3.4. We use linear plots to give a clear indication of the dissipation. First, consider Fig. 3.4B. Lee waves are stationary waves by definition, and thus have a frequency of zero in a Eulerian frame of reference. Hence, the spectra peak at zero frequency, where it has an amplitude of 6.4 $\times$ 10−3 m^{2}s for the bottom depth level. By the time they reach the 1400 m depth level, 5% of the original signal is left. This is in line with findings by Nikurashin and Ferrari (2011) and Nikurashin, Vallis, and Adcroft (2013), who found that lee waves decayed in the bottom ocean (the bottom 2 km of the ocean). At the 100 m depth level, spectral density is of the same order of magnitude, which is likely due to flow trapping, which will be discussed in more detail later.

In Fig. 3.4S, the spectral density for run S is plotted, centred around the inertial frequency. Because near-inertial waves are mostly generated by surface forcing, and wind stress in particular, the strongest signal is at the 100 m depth level. The kinetic energy at the

3200 m depth level is 90% of the original signal, and 75% at 1400 m. Near-inertial waves thus decay less quickly than lee waves. The decay rate is line with the literature, and the suggestion by Wunsch and Ferrari (2004) that near-inertial waves might be a good candidate for deep ocean mixing. At the 100 m depth level, the near-inertial peak is slightly offset to the left of the inertial frequency. At 1400 m, the near-inertial peak is at the near-inertial frequency, and at 3200 m, it slightly offset to the right. This spread of peak frequencies is likely due to high relative vorticity near the surface, setting the effective inertial frequency to less than f, thereby allowing waves to be generated over a slightly larger range. As the wave propagate downward, the relative vorticity decreases over all space horizontally, increasing the effective inertial frequency over all space horizontally, and thereby causes dissipation of near-inertial waves above the new effective inertial frequency.

Brearley et al. (2013) also investigated the internal wave field in the Scotia Sea, but by observation. The latitude of the mooring site ranged from 56° 5' S to 55° 57' S. At 56° S, the near-inertial and the M_2 tidal frequencies are very close to each other. The near-inertial frequency is $f = -1.206 \times 10^{-4}$ s^{-1}, while the M_2 frequency is 1.405×10^{-4} s^{-1}, giving a ratio of $|f|/M_2 = 1.17$. Hence, it is difficult to distinguish these signals. Due to the resolution used in Brearley et al. (2013), the near-inertial peak was approximately two frequency steps removed from the M_2 frequency. Without a method to distinguish the two, they conclude that the peak is mainly due to the near-inertial signal. However, with better frequency resolution, the results from this model suggest that the M_2 internal tide is dominant, being about an order of magnitude larger near the bottom of the ocean. Even at 100 m depth, we find that the M_2 internal tide has greater horizontal kinetic energy than near-inertial waves.

In Fig. 3.5, the spectral density for run T is plotted. Since run T is the most realistic of the runs, this is the most comparable graph in this work to the kinetic energy spectral density of Brearley et al. (2013). However, Brearley's spectral density plot shows the total kinetic energy, while Fig. 3.5 shows the wave kinetic energy. Fig. 3.5 has a clear lee wave signal with an amplitude at 0 frequency of $2 * 10^{-3}$ m^{2}s. However, the maximum lee wave amplitude is two orders of magnitude smaller than the M_2 peak at the 3200 m depth level. Two peaks occur at tidal frequencies O_1 and K_1, despite that O_1 and K_1 being sub-inertial. For wave propagation we require $f^2 < \sigma^2 < N^2$. However, this does not imply that internal waves cannot be generated below the inertial frequency. When they are, they simply dissipate very quickly after. This result underscores the importance of using the Lagrangian frame of reference for the analysis of internal waves. Further along the spectrum, we find the near-inertial peak (depicted with a yellow line) and the M_2 peak, as discussed above. Before the harmonics of M_2 and the other semi-diurnal frequencies, we find a peak of the same order of magnitude as the K_1 peak at $M_2 + K_1$.

Surprisingly, despite the fact that internal tides are generated near the seafloor, and despite the spectral density being divided by N, the spectral density at 3200 m at the semi-diurnal frequencies and above is less than the spectral density at 1400 m, which in turn is less than at 100 m. Lee waves, on the other hand, follow the expected pattern of having highest spectral density at 3200 m, less at 1400 m, and still less at 3200 m. This suggests that the internal tides are subject to a process that lee waves are not, or at least not to the same degree. The likely explanation for the spectral density increasing away from the bottom is that due to Doppler shifting, the M_2 internal tide becomes flow trapped. The Doppler shift increases away from the seafloor. Hence, the elevated kinetic energy with height is possibly due to trapped waves inducing a reservoir of kinetic energy near the

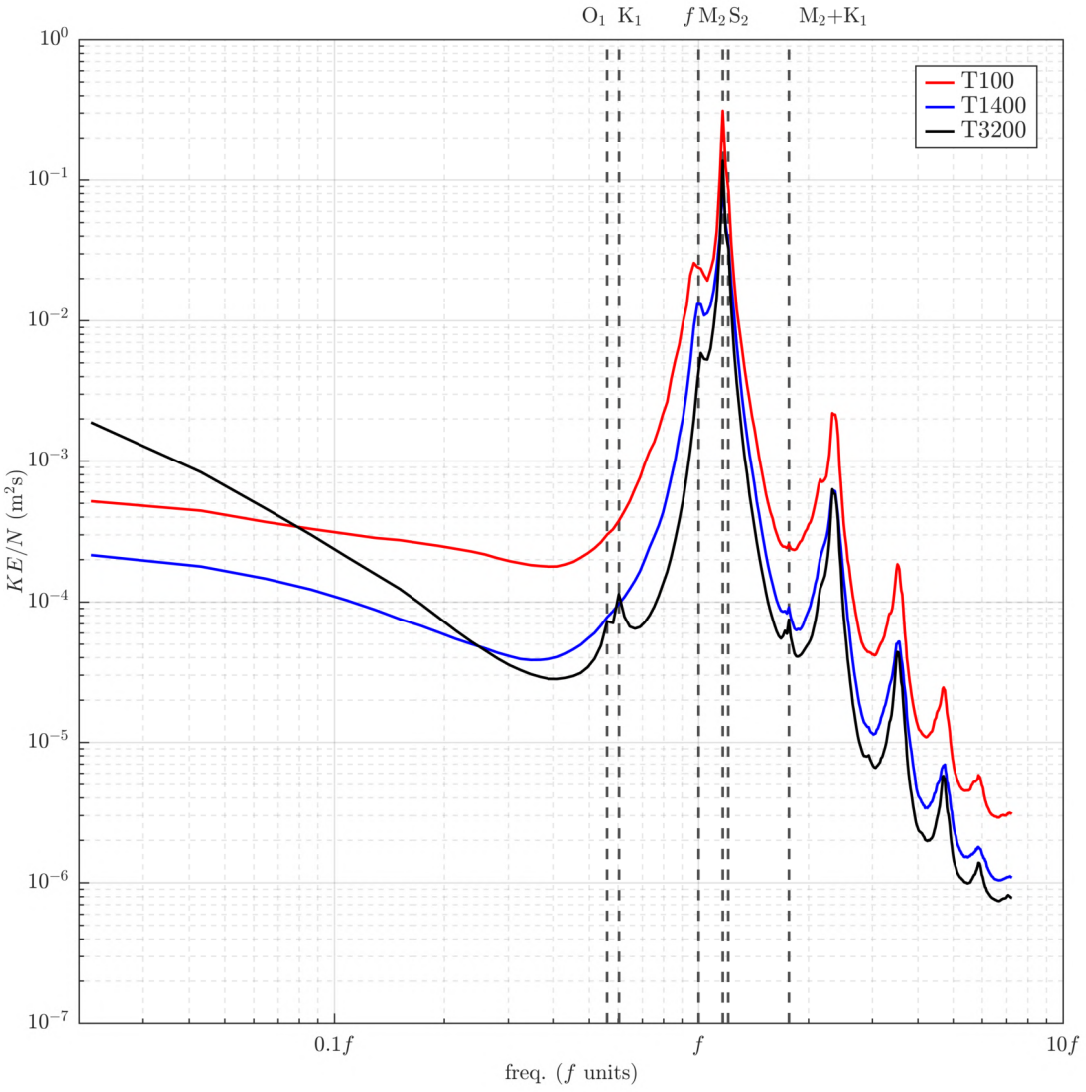

Figure 3.5: Comparison of the wave kinetic energy vs frequency of the three runs at each depth level. The peak at zero frequency of run B is due to lee waves. The highest peak for run S is at the inertial frequency f, and each subsequent peak for run S is a harmonic of the inertial frequency. The highest peak for run T is the M_2 the internal tide, of which the harmonics can also be observed. The local maximum to the left of the inertial peak is the K_1 internal tide.

surface.

3.4 Temporal variability

In this section, we will consider temporal variations in the N-scaled kinetic energy of the internal wave field. To obtain a global overview of the temporal variability, the scaled kinetic energy spectral density has been plotted as a function of frequency and time for the domain of interest in Fig. 3.6. To obtain the kinetic energy as a function of frequency and time with high frequency resolution, a four-week window was taken surrounding each point in time, and taking the Fourier transform in time of the already Lagrangian filtered variables over that window. The higher frequency resolution comes at the cost of increasing the time window, which effectively means that each point in time is a 28-day moving average. This frequency resolution is 2.6×10^{-6} s-1, which is necessary to accurately distinguish the M_2 signal from the near-inertial signal.

From Fig. 3.6, it is apparent that there is both seasonality in the signal, as well as multi-day events. Consider Fig. 3.6B3200 first, where lee waves dominate the spectral density. For this run, there is little seasonality in the signal, but there are multi-day events. From approximately 50 to 100 days, there is a strong spectral density signal. Another high generation period occurs later from approximately 150 days to 180 days with a peak not from the zero frequency to 2.6×10^{-6} s-1, but from 2.6×10^{-6} s-1 to 5.2×10^{-6} s-1. The frequency implies that this is a lee wave signal. This suggests that strong Doppler shifting is present. Another period of high generation spans 260 to 320 days. Given that each point is a 30-day moving average, it is unknown whether these three periods of high lee wave generation is due to multiple events or a sustained event. As can be seen in B1400 and B100, lee wave spectral density decreases with depth for each of the three events.

In Fig. 3.6S100, we can see a clear near-inertial signal. The frequency band to the right of the near-inertial band is a harmonic at $2f$. And to the left we find a clear lee wave signal, which increases in energy with depth in S1400 and S3200. Because of the narrow frequency band over which the tides have kinetic energy, it is difficult to see see the temporal variability in this figure. Therefore, we integrate the kinetic energy over the bands and show it on a line plot later.

In Fig. 3.6T100-T3200, we can see the same wave types as in run B and S, and distinguish three peaks from different internal tides (actually five, but O_1 and K_1, and M_2 and S_2 are too close together to distinguish them in this plot). These are the diurnal internal tides, near-inertial waves, and the semi-diurnal internal tides, respectively. The near-inertial band can be seen just slightly to the left of the M_2 tidal peak. To analyse this data further, we will integrate the kinetic energy over lee waves, spontaneously generated waves, near-inertial waves, and each of the internal tides.

In Fig. 3.7, the scaled kinetic energy integrated over the lee wave frequency band is plotted for B100. Along the frequency dimension, the scaled lee wave kinetic energy decreases until a near-inertial kinetic energy signal begins to appear, which is just after the local minimum of 1.12×10^{-4} s^{-1}. For lee waves, the average scaled kinetic energy was integrated from zero frequency up to this local minimum. There are three clear periods of high generation. According Bell (1975a), lee wave generation is mainly a function of bottom flow velocity. To check this, we correlate the lee wave kinetic energy with the bottom flow velocity. As discussed earlier, the 28-day window for the time Fourier transform by which we obtained the scaled kinetic energy in the frequency-time domain implies that effectively we have a

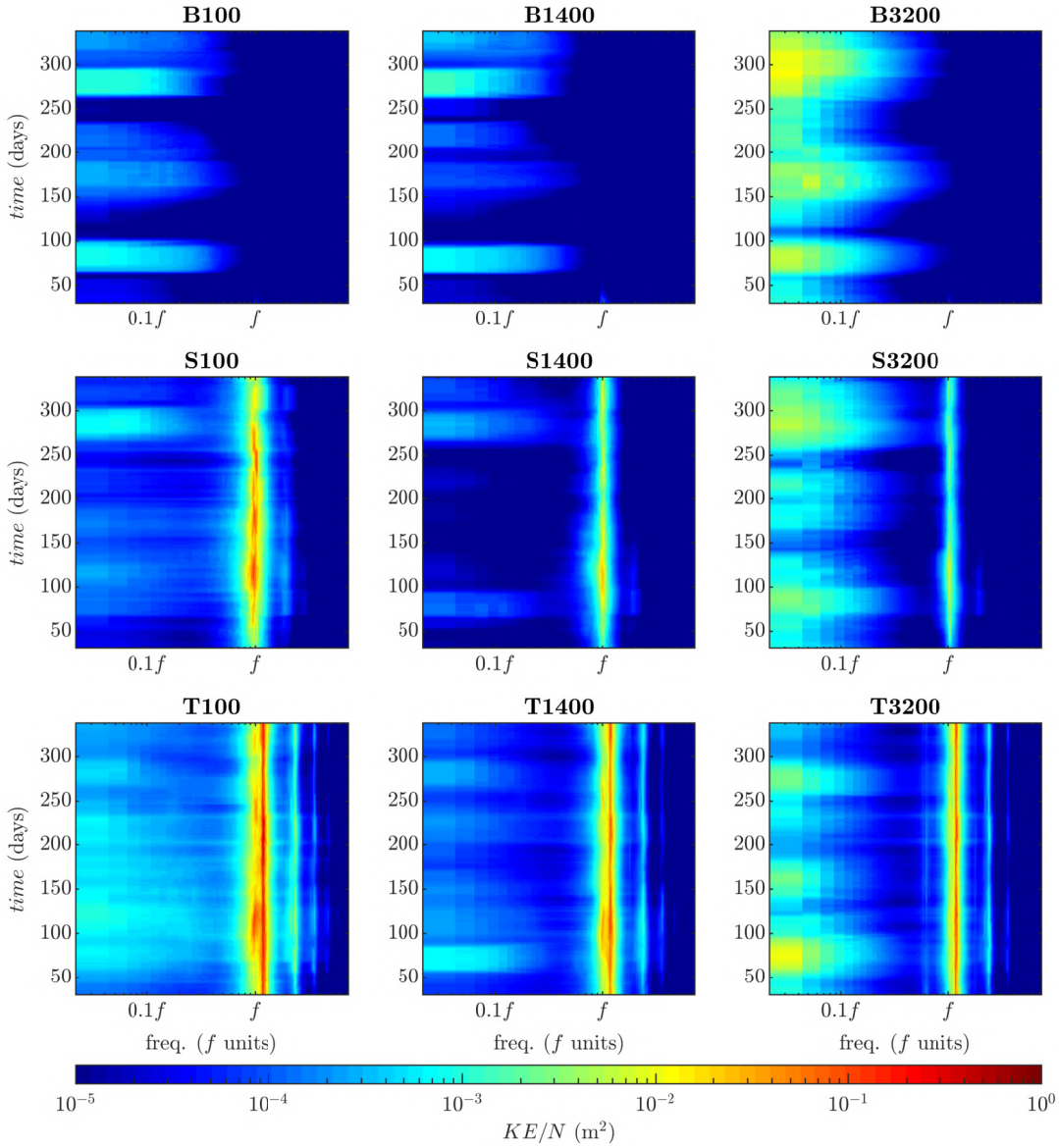

Figure 3.6: The horizontal wave kinetic energy as a function of frequency and time for all runs and depth levels. Note that the signal through time is a 28-day moving average due to having a 28-day moving time window for the Fourier transform in time to produce this plot. This is necessary to clearly distinguish the near-inertial signal from the M_2 internal tide.

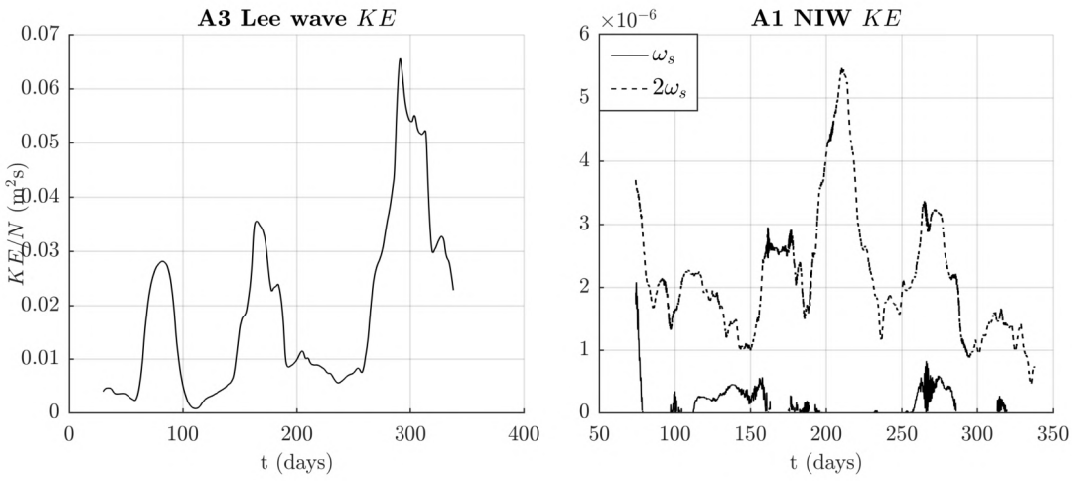

Figure 3.7: Lee waves and trapped lee waves for run B. The graph on the left is scaled lee wave kinetic energy, measured at the 3200 m depth level, while on the right is the near-inertial signal (note that it is much smaller than the lee wave signal) at the 100 m depth level.

28-day moving average. Correlating this signal with the bottom flow velocity gave a poor correlation coefficient.

Fortunately, the difference between the scaled kinetic energy over the whole spectrum and the lee wave integrated kinetic energy is negligible. Hence, to check the effectiveness of linear theory for lee waves, we correlate the spatial average of the wave kinetic energy for run B, which is effectively the lee wave kinetic energy. The normalised wave kinetic energy at each depth level, as well as the normalised bottom flow velocity, are plotted in Fig. 3.8. Our results are in good agreement with linear theory with a cross-correlation coefficient at the 3200 m depth level of 0.81 with a 0 ± 0.5 day lag (the bottom flow velocities have a time resolution of 1 day). In addition, we find that for the for 1400 m depth level, the correlation was 0.71 with a 1 ± 0.5 day lag, and for the 100 m depth level, also a correlation of 0.71 but a 2 ± 0.5 day lag. Hence, the the average vertical group speed of lee waves is approximately $\Delta x/\Delta t = 3100$ m /48 hours $= 7 \times 10$ m/hour.

In the right panel of Fig. 3.7, the near-inertial signal has been plotted. This was obtained by taking a frequency band around the inertial frequency. Since the lee wave energy declines with frequency, there was a local minimum to the left of the near-inertial frequency peak. We took the difference between the frequency of the local minimum and the peak frequency and multiplied that by two to give a band around the near-inertial frequency. The mean lee wave signal across this band is found by taking the kinetic energy at the frequency directly to the left and the right of the band, and taking the average of those two. This is subtracted from the average kinetic energy over the near-inertial band. In the right panel of Fig. 3.7, the solid curve indicates the fundamental frequency, and the dashed curve the first harmonic. One possibility for the signal at the near-inertial frequency is described in Nikurashin and Ferrari (2010). As lee waves break, they deposit their momentum to the mean flow. The momentum decreases the amplitude of the mean flow, and induces near-inertial waves, similar to wind stress at the ocean surface.

Run S has strong near-inertial wave generation, mainly wind-generated. This scaled kinetic energy in this frequency band is shown in Fig. 3.9. Like Danioux et al. (2011), we find

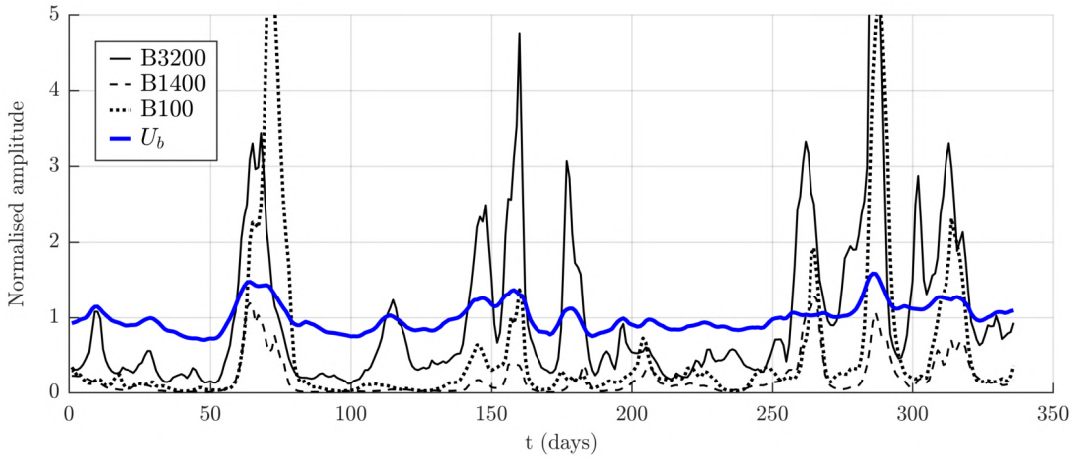

Figure 3.8: Normalised bottom flow speed and normalised lee wave kinetic energy for the boundary forced run. The bottom flow speed is normalised by the mean of the bottom flow speed. The lee wave kinetic energy at every depth level is normalised by the mean of lee wave kinetic energy at the bottom. Note that the kinetic energy is not divided by N here. Hence, with increasing height, the wave slope becomes more horizontal, giving the waves more horizontal kinetic energy.

a harmonic at $2f$. In their study, Danioux et al. first run their model for 450 days to allow mesoscale eddy energy to achieve statistical equilibrium, and build up a mixed layer. After also applying some surface forcing except for wind for a period of 10 days to obtain a stable mixed layer depth, they apply a wind forcing uniformly to the whole domain for 20 days. Unlike their simulation, we find that the peak at the harmonic is approximately two orders of magnitude smaller at any point in time. This run has signs of both seasonality and multi-day events. Due to the waves requiring approximately 100 days to reach the ocean bottom, it is difficult to distinguish the initialisation signal from the real signal. However, the spatial average shown in Fig. 3.9b, which is not a moving average, the signal appears very different. The moving average smooths the peaks, and better shows the initialisation effect. However, after a peak occurs at 118 days, it is not clear when the initialisation phase is over. At minimum, it seems to be approximately 150 days, but it is possible that it takes much longer to stabilise. To investigate this further, the model needs to be run for a longer period of time. However, it is clear from this signal that there are many multi-day events, which for peaks larger than the mean range from about one week to about three weeks. These are likely associated with periods of sustained high winds, such as during storms. Regarding the harmonic $2f$, note that it largely follows f, except during the initialisation period. However, while each of the peaks in f are of the same order of magnitude, they become increasingly small for $2f$.

Correlating the spatial mean surface wind stress τ with the spatial mean kinetic energy gives a cross-correlation coefficient of 0.38 for the domain of interest and a lag of 80 hours, which is 3 days and 8 hours. This gives an average vertical group speed of 1.25 m/hr between the surface and the 100 m depth level. Assuming this is constant across depth, it would take approximately 100 days for the waves to reach the bottom depth level. To show the correlation, both the mean surface wind stress and the mean kinetic energy at 100 m for the surface forced run have been plotted in Fig. 3.10, where the S100 signal has been shifted backwards in time to match the predicted lag. The wind stress is very

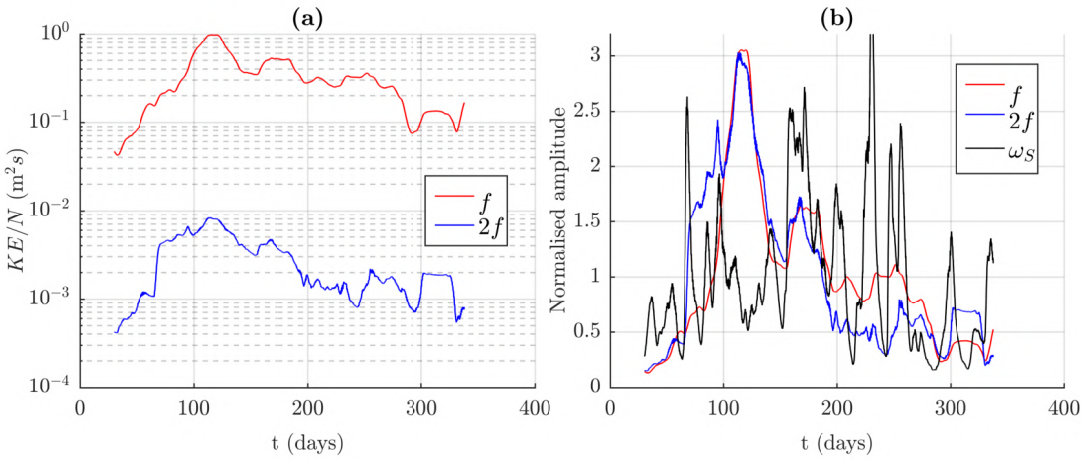

Figure 3.9: Scaled kinetic energy in the near-inertial wave band (left) and mean-normalised scaled kinetic energy in the near-inertial wave band on the right. Label f refers to the frequency band around f, $2f$ around $2f$, and ω_S is the spatial average of the scaled kinetic energy for run S. Since nearly all kinetic energy is in the f band, the spatial average effectively shows the kinetic energy in f. The difference is that the f band is effectively a 28-day average, while the spatial average is instantaneous kinetic energy. The y-axis for (b) is in units of each signal's mean.

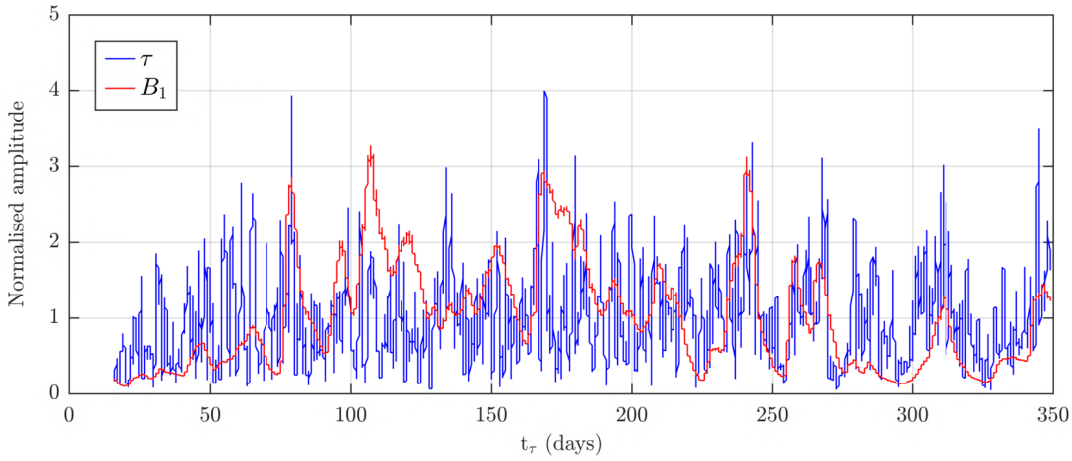

Figure 3.10: Mean-normalised near-inertial wave kinetic energy and surface wind stress τ. The y-axis is thus in units of each signal's mean.

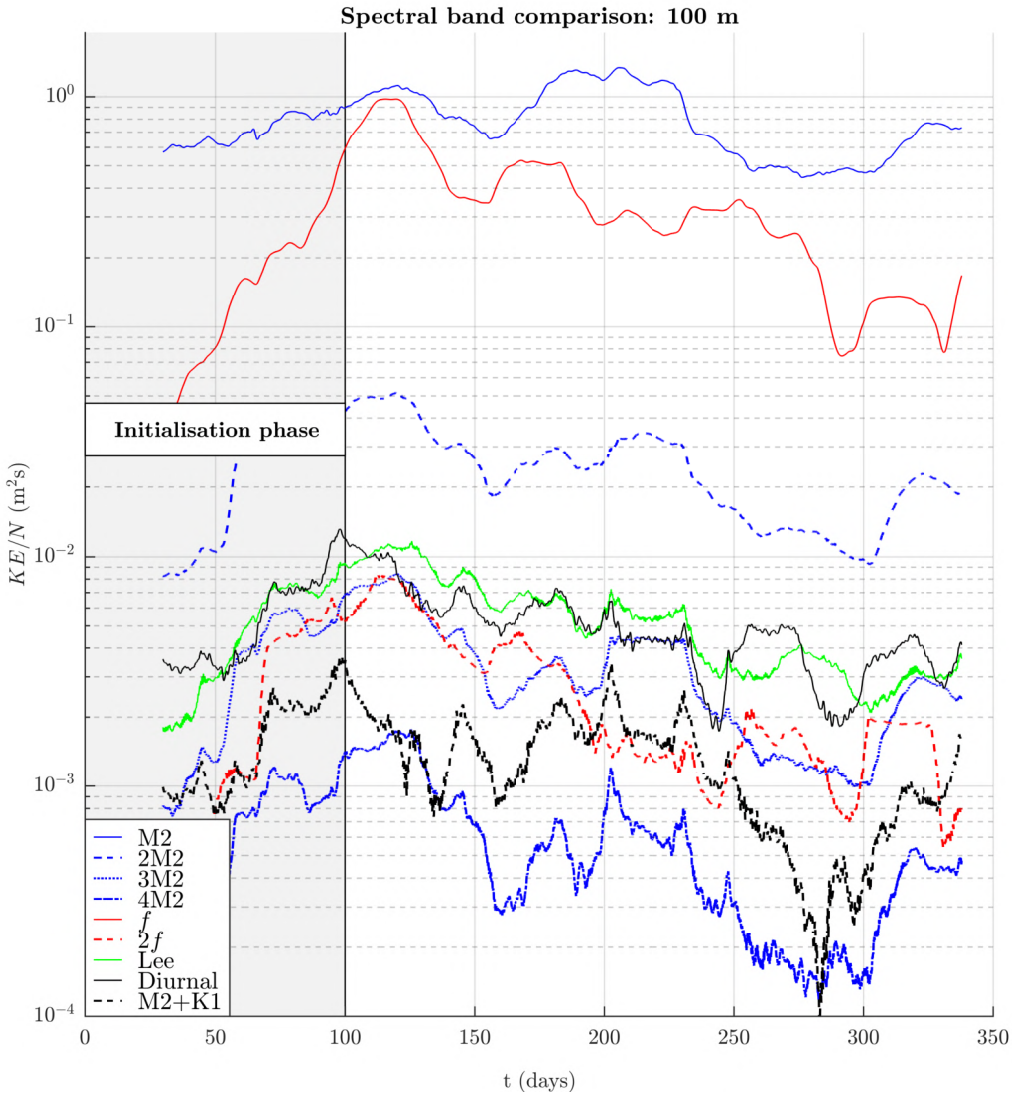

Figure 3.11: The kinetic energy scaled by N for different types of waves and frequency bands across which the scaled kinetic energy was integrated at 100 m. Note the the near-inertial signals were taken from run S. All other signals were found by partitioning the frequencies in run T.

noisy. For the first 70 days, the correlation coefficient is 0.54, higher than for the whole time period. The reason that the cross-correlation coefficient decreases with time is likely that near-inertial waves become flow trapped, causing the kinetic energy to be noisy at later times.

To show the relative magnitudes and the variation of the internal wave field near the surface, the middle, and the bottom, each wave type has been plotted in Fig. 3.11, 3.12, and Fig. 3.13. In Fig. 3.11, the scaled kinetic energy for different types of waves are plotted for the 100 m depth level. Despite being close to the surface, the M_2 internal tide is the strongest here, ranging from 4×10^{-1} to 1 m^{-1}, which are separated by a factor of 2.5. The near-inertial band has a minimum of 7×10^{-2} m^2s and maximum of 1 m^2/s, which is more than an order of magnitude difference. The strength of the M_2 internal tide relative to near-inertial waves is surprising. It seems likely that this is due to flow trapping of the M_2 internal tide near the surface, creating a reserve of kinetic energy near the surface.

The M_2 signal at 100 m fluctuates much less than the near-inertial signal. The reason for this difference is that the M_2 tide is dependent on the barotropic tides, which are dependent on the lunar cycle, and thus provides a fairly constant source of energy, while the near-inertial waves are mostly induced by wind stress near the surface, which is largely dependent on the season, as well as weather events. In addition, the initialisation phase increases the variability in time. The propagation of the internal tides is dependent on N. It appears that the strength of the signal of M_2 near the surface is partly controlled by the stratification in the middle of the ocean. The first harmonic of the M_2 frequency varies very similarly to the M_2 signal, and the same is true for the second and third harmonic. The $2M_2$ harmonic ranges from 9×10^{-3} to 5×10^{-2} m^2s, thus varying more than the principal frequency.

The other frequency bands make only a small contribution to the scaled kinetic energy in the internal wave field at 100 m depth. In particular, lee waves here are insignificant, as they have largely decayed. The near-inertial and the M_2 frequency bands dominate the internal wave field at 100 m in the Scotia Sea. Second to third-order contributions are made by the $2M_2$ harmonic.

The spectral bands at the 3200 m depth level are plotted in Fig. 3.12. The near-inertial signal here is more than an order of magnitude smaller, as expected. Lee waves are are somewhat more significant, though at any point in time, other than during spin-up, they are more than an order of magnitude, sometimes two orders of magnitude, smaller. Note that the lee wave signal here is different from that shown in earlier figures due to the above being the lee wave signal in forcing regime B, while here the lee wave signal is that measured for run T. The near-inertial signal here, despite being generated near the surface, is larger than that lee wave signal. The first harmonic of the M_2 internal tide is comparable to lee waves, though again, with less fluctuation. The harmonics of M_2 vary more, however. The fundamental frequency band keeps in between 3 m^2/s and 4 m^2/s, the first harmonic between 0.03 m^2/s and 0.9 m^2/s, the third harmonic between 0.004 m^2/s and 0.01 m^2/s, and the fourth harmonic between 7 $\times 10^{-3}$ m^2/s and 2 $\times 10^{-2}$ m^2/s.

Regarding the $3M_2$ band, the M_2+K_1 band, and the K_1 band, there is an interesting interplay between them through time. First, there is an initialisation period. In the first 30 days, the signals decrease. After the initialisation period, initially the $3M_2$ band is at approximately three times the kinetic energy of the other two bands, while the M_2+K_1 band and the K_1 band are largely on top of each other. Then the three signals converge,

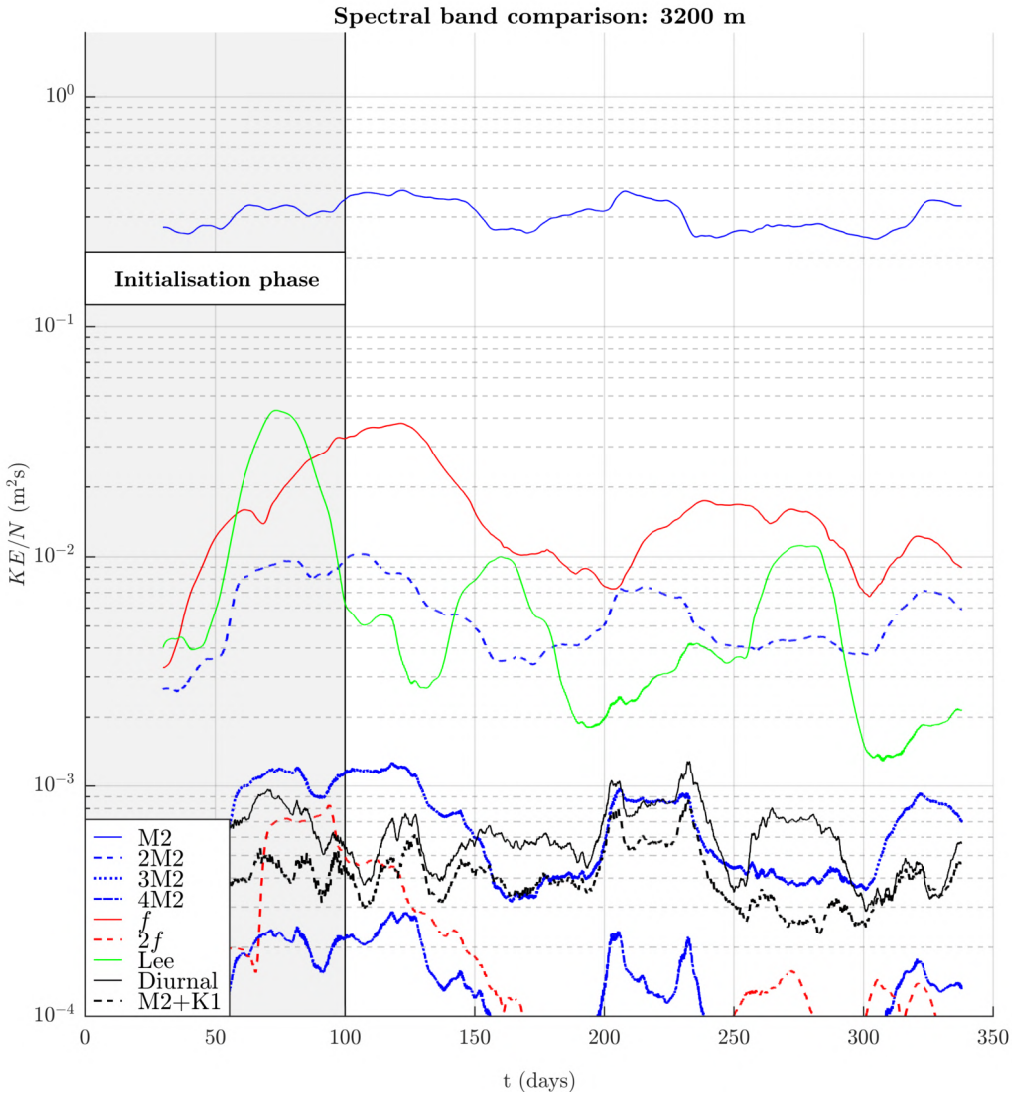

Figure 3.12: The kinetic energy scaled by N different types of waves and frequency bands across which the energy was integrated at 3200 m. Note the the near-inertial signals were taken from run S. All other signals were found by partitioning the frequencies in run T.

but just before they touch, the K_1 frequency band gains more kinetic energy than the other two, now having more than $3M_2$ signal. Around 200 days, the signals converge again, due to K_1 losing energy. The M_2+K_1 is generally the lowest, except for a period near the end, where the K_1 band is the smallest. The $3M_2$ and K_1, however, often diverge and converge, while also having some period where they have largely the same amount of kinetic energy. In summary, it seems that the $3M_2$ band, the M_2+K_1 band, and the K_1 band have underlying variables that drive these convergences and divergences of their kinetic energy. One reason might be wave-wave energy exchanges between these bands. The fact that the K_1 is trapped, while M_2 is not is also likely to play a role, with variables such as the local Doppler shift and the relative vorticity influencing the temporal variation. This requires further investigation.

The $4M_2$ signal here is negligible to any of the others, as well as the $2f$ band. Near the bottom in the Scotia Sea, the M_2 internal tide dominates the N-scaled kinetic energy spectrum at all tides, with only a second to third-order contribution by the near-inertial, lee wave, and $2M_2$ frequency bands. Combined, however, these last three can still contribute a first-order kinetic energy contribution. Finally, the interplay between the $3M_2$ band, the M_2+K_1 band, and the K_1 band requires further investigation.

Now we consider the depth level at 1400 m, in between the two generation depth levels. The N-scaled kinetic energy is plotted Fig. 3.13. At this depth level, the scaled kinetic energy in the M_2 band is approximately an order of magnitude larger than near-inertial band. The M_2 band ranges from 0.2 to 0.5 m^2s , while the near-inertial band ranges from 7×10^{-3} to 4×10^{-2} m^2s. The next most significant frequencies are 1 to 2 orders of magnitude smaller. Only the $2M_2$ band occasionally has second-order effects at times. The harmonics of M_2 all largely follow the same pattern again as the fundamental frequency. At this level, it appears that the $3M_2$+K_1 frequency band correlates well with M_2 frequency band (or its harmonics). Whether it is the harmonics that control the energy in this band or the fundamental frequency requires further investigation.

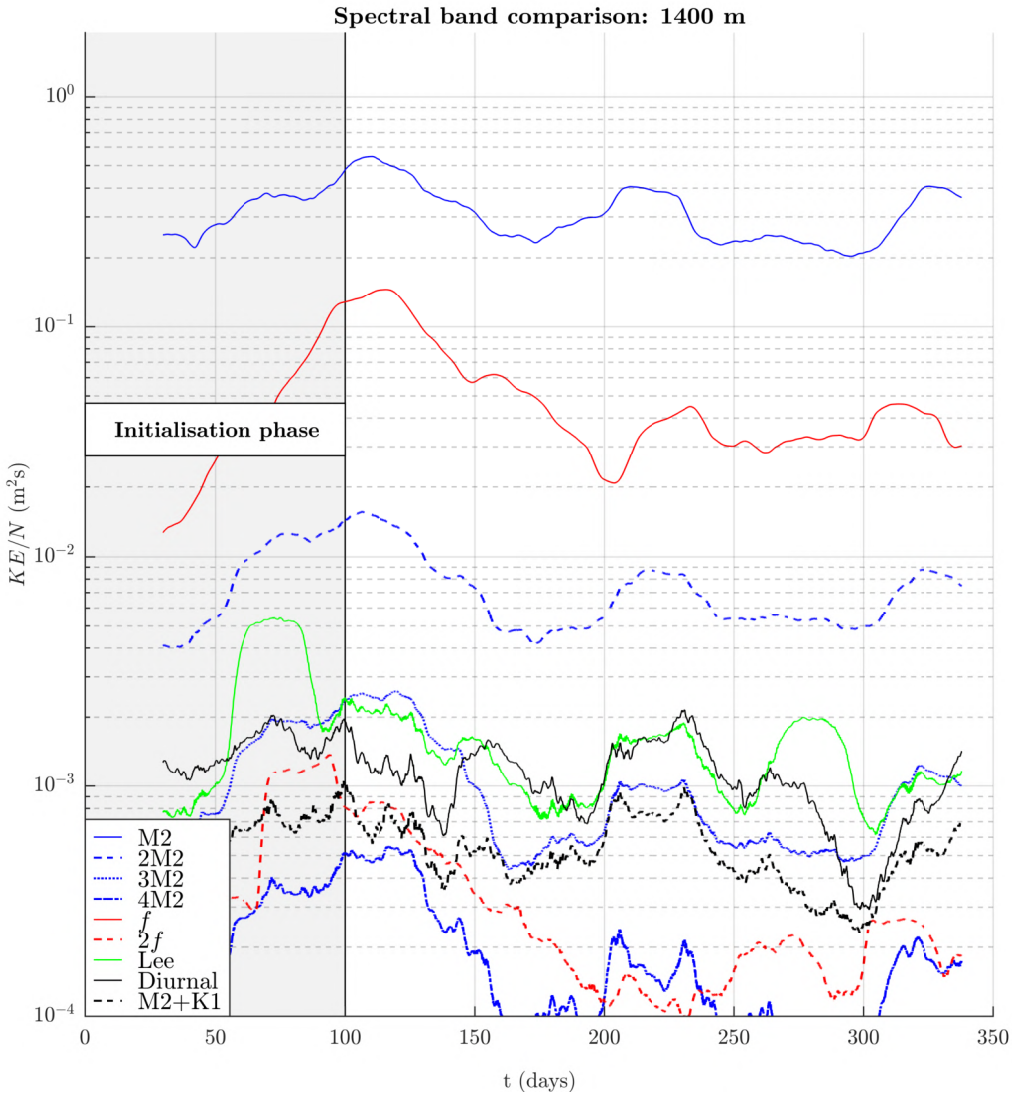

Figure 3.13: The kinetic energy scaled by N different types of waves and frequency bands across which the energy was integrated at 1400 m. Note the the near-inertial signals were taken from run S. All other signals were found by partitioning the frequencies in run T.

Discussion

This work found and characterised the different types of waves present in the Scotia Sea in the Southern Ocean, and examined the spatial and temporal variation of the internal wave field, and the implications for deep ocean mixing. There are a number of idealised studies that have investigted the generation and propagation of internal waves, such as Nikurashin, Vallis, and Adcroft (2013), Shakespeare and Taylor (2015), and Yang et al. (2018). Various observational studies have investigated the internal wave field, such as Brearley et al. (2013), or a combination of a model with observations by satellite altimetry, such as by Alford et al. (2019). There are only a small number of papers that employed high resolution numerical ocean models to directly model the generation and propagation of internal waves. Rayson et al. (2011) employed a realistic model with variable resolution with a resolution of 1 to 3 km in regions of internal wave generation to investigate internal tide generation on the continental shelf. Mashayek et al. (2017) ran a high-resolution ocean model for 250 days to quantify vertical turbulent mixing by using numerical tracers. Rath, Greatbatch, and Zhai (2014) investigated the spatiotemporal variability of near-inertial waves in the Southern Ocean using a lower resolution $(1/10)^\circ$ model for more than thirty years. However, to the author's knowledge, no earlier work has examined the spatiotemporal variability of the internal wave field in a high resolution model under a realistic forcing regime, which gives this work unprecedented insight into the internal wave field present in the Southern Ocean, and the Scotia Sea in particular. In addition, the model was run for one year, which enabled the quantification of the temporal variability in the different wave types, which at present is poorly constrained. Finally, this work used a unique and novel filtering technique (see section 2.3) to rigorously separate the wave component of the flow from the nonwave component, which made it possible to quantify the kinetic energy in the three wave types that are thought to be the main sources of deep ocean mixing.

In Fig. 4.1, the mean and standard deviation of the scaled kinetic energy in time for each wave band is plotted at the 100 m, 1400 m, and 3200 m depth levels. The key wave types are the M_2 internal tide, near-inertial waves (NIW), and lee waves. Below we will discuss the main findings in detail.

4.1 The M_2 internal tide

In our model, out of all wave types analysed, the M_2 internal tide has the largest N-scaled kinetic energy in the internal wave field at all depth levels in the Scotia Sea. Near the bottom of the Scotia Sea, at 3200 m depth and excluding the initialisation phase, the M_2 internal tide had a mean value of 0.31 m^2/s, while near-inertial waves had a mean value

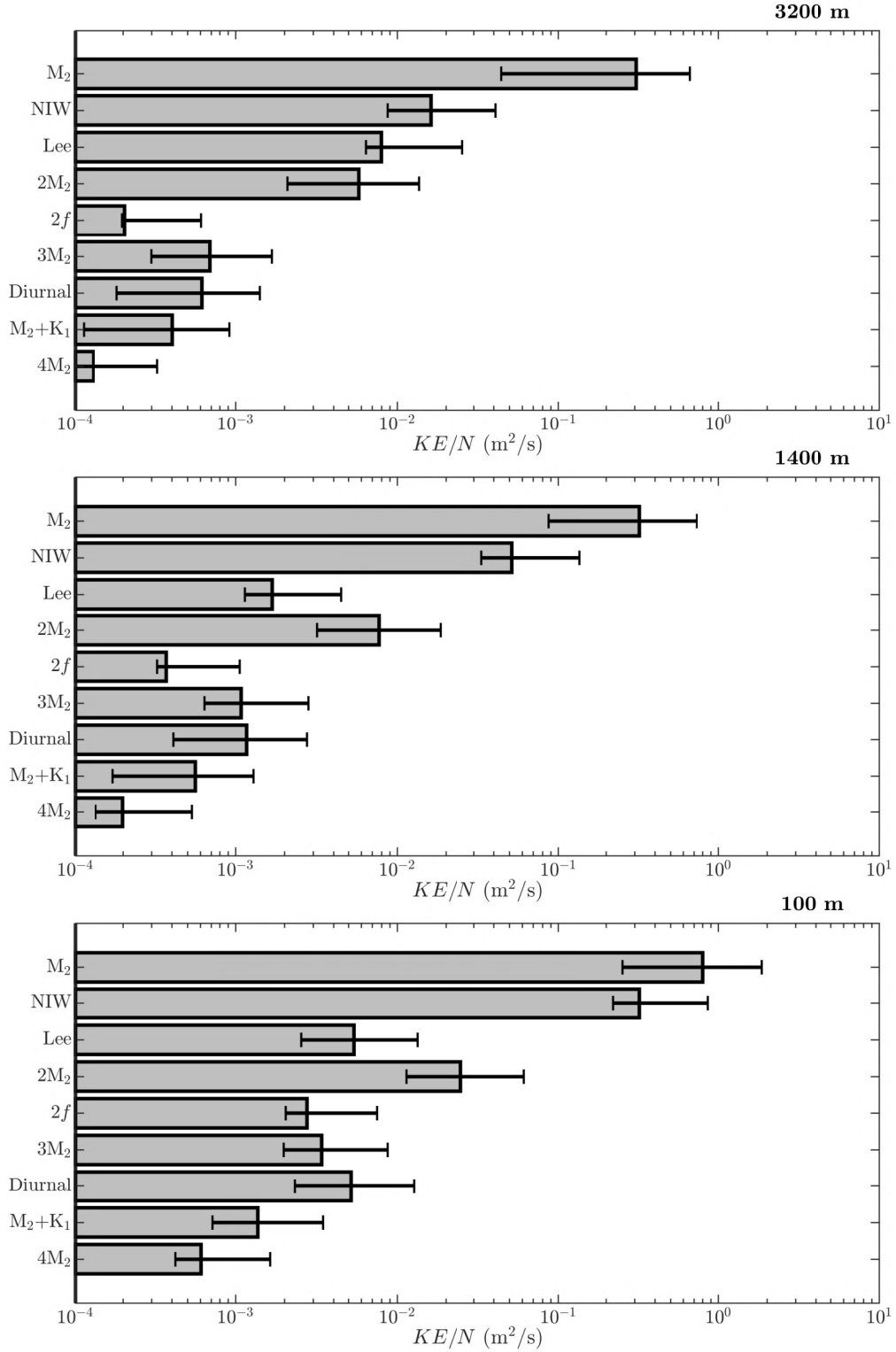

Figure 4.1: Scaled wave kinetic energy at 3200 m, 1400 m, and 100 m depth. The mean buoyancy frequency N at each of these depth levels was 0.0065 s^{-1}, 0.0067 s^{-1}, and 0.0076 s^{-1}, respectively.

of 0.016 m^2/s, lee waves had a mean value of 0.0046 m^2/s, and the $2M_2$ harmonic had a mean value of 0.0055 m^2/s. The M_2 internal tide has the largest amount of kinetic energy at this depth, having one order of magnitude more scaled kinetic energy than the next largest wave type. This result implies that the M_2 internal tide has the most potential to transfer kinetic energy to deep ocean mixing in the Scotia Sea.

In our model, there is significant temporal variability in the M_2 internal tide in the Scotia Sea. Excluding the initialisation phase, the M_2 internal tide had a standard deviation of 0.048 m^2/s which is 15% of the mean. Given that the Fourier transform of the Lagrangian filtered kinetic energy used a 28-day moving time window, the output is essentially a moving average of 28 days. The maximum and minimum values reported here are thus a lower bound on the variability; if the signal could be directly observed, the minimum value would be lower and the maximum value would be higher. The significant temporal variability in the M_2 internal tide implies that any observation that quantifies the kinetic energy in the M_2 internal tide over some period gives the kinetic energy only for that particular period, and cannot be assumed to be representative of the signal throughout the year. On a technical note, our result above underscores that it is not always preferable to maximise the moving time window over which the Fourier transform in time is taken. Reducing the time window results in better time resolution in time-frequency space but worse frequency resolution, while increasing it results in better frequency resolution but worse time resolution. For this work, it was important to distinguish the M_2 internal tide from near-inertial waves, which is why a relatively longer moving time window was chosen.

4.2 Near-inertial waves

In our model, near-inertial waves make the second largest contribution to the scaled kinetic in the internal wave field in the Scotia Sea at 100 m and 1400 m depth, and the fourth largest at 3200 m depth. At 100 m depth, near-inertial waves had a mean value of 0.36 m^2/s, while the M_2 internal tide had a mean value of 0.82 m^2/s, and the $2M_2$ harmonic had a mean value of 0.025 m^2/s. Lee waves, diurnal frequencies, the near-inertial harmonic, and the $3M_2$ harmonic all have scaled kinetic energy of an order of magnitude or more smaller than the $2M_2$ harmonic. The Southern Ocean is known to have strong winds, so it is expected that near-inertial waves have scaled high kinetic energy in the Scotia Sea. However, it is surprising that near-inertial waves have less mean scaled kinetic energy than the M_2 internal tide. Brearley et al. (2013) conducted an observational study of the Scotia Sea to investigate the eddy contribution to enhanced deep ocean mixing in the Southern Ocean. Though not the focus of their study, the strong peak that occurs close to f was attributed to near-inertial waves. At 56° S latitude, the inertial frequency $f = 1.2 \times 10^{-4} s^{-1}$, while the M_2 internal tide has a frequency of $1.4 \times 10^{-4} s^{-1}$. High frequency resolution is necessary to be able to distinguish near-inertial waves from the M_2 internal tide at this latitude. By running our model for one year, and using a 28-day moving time window, and having a separate surfaced case from a surface and tidally forced case, we were able to clearly separate the relative contributions made by the near-inertial wave band and the M_2 internal tide. Given the near inertial waves' relatively large scaled kinetic energy at the 100 m depth level, near-inertial waves have less than but comparable potential to to the M_2 internal tide to transfer transfer kinetic energy to mixing near the surface in the Scotia Sea. However, at the 3200 m depth level, the relatively low mean scaled kinetic energy in the near-inertial wave band internal tide implies that, on average,

it has little potential to transfer significant amounts of kinetic energy to deep ocean mixing compared to the M_2 in the Scotia Sea.

In our model, near-inertial waves also have strong temporal variability in the Scotia Sea at all depth levels. Based on the Fourier transform in time of the Lagrangian filtered kinetic energy, at 100 m depth, excluding the initialisation phase, near-inertial waves had a standard deviation in time of 0.22 m^2/s, which is 63% of the mean (0.36 m^2/s). It achieved a maximum scaled kinetic energy of 0.97 m^2/s, and a minimum value of 0.075 m^2/s. The scaled near-inertial kinetic energy over the full year thus varies by more than one order of magnitude. Unlike the M_2 internal tide, for near-inertial waves we have both the moving average of the scaled kinetic energy and the instantaneous scaled kinetic energy with two qualifications. First, the instantaneous scaled kinetic energy is over all frequencies rather than just the near-inertial band. However, from the Fourier transformed signal, we found that nearly all kinetic energy in run B is in the near-inertial band. The difference between the total kinetic energy in run B and the near-inertial band is negligible. Second, the instantaneous values were found to be approximately a factor of π smaller than the Fourier transformed kinetic energy. The instantaneous scaled kinetic energy was found to have peaks throughout the year where it was near to or greater than the maximum value found in the Fourier transformed kinetic energy. At the 100 m depth level, despite the fact that near-inertial waves have a mean value that is smaller than the M_2 signal, during storms near-inertial waves can have have greater scaled kinetic energy than the M_2 internal tide. Therefore, even more so than for the M_2 internal tide, observations of near-inertial waves for periods of time shorter than one year are not representative of the signal throughout the year in the Scotia Sea, and likely in other regions too. Even at the 3200 m depth level, peaks occurred which were approximately 20% of the M_2 internal tide mean.

4.3 Lee waves

Lee waves make the third largest contribution of scaled kinetic energy to the internal wave field at the 3200 m depth level in our model, and the fourth largest at the 1400 m and 100 m depth level. At the 3200 m depth level, excluding the initialisation phase, lee waves had a mean scaled kinetic energy value of 0.0046 m^2/s. This is a surprising result. Lee waves are thought to be a major source of deep ocean mixing in the Southern Ocean (e.g. Nikurashin, Vallis, and Adcroft (2013)). One reason might be that earlier literature has quantified lee wave generation in idealised case studies and by using linear theory. No previous works have directly modelled lee waves in a high-resolution, wave-permitting regional model under a realistic forcing regime. The relatively small contribution of scaled kinetic energy to the internal wave field by lee waves in our model suggest that lee waves might only make a small contribution to deep mixing. However, running a model with a realistic forcing regime at higher resolution would more completely resolve the internal wave spectrum and other smaller scale processes. Lee wave generation is known to be sensitive to rough, small-scale topography and thus it is possible that higher spatial resolution increases lee wave generation.

The temporal variability of lee waves in our model at 3200 m depth was as strong as the temporal variability in near-inertial waves at 100 m depth. Excluding the initialisation phase, lee waves had a standard deviation in time of 0.0029, which is 63% of the mean (0.0046 m^2/s). It has a correlation coefficient of 0.81 with the deep ocean mean flow in the model, which corresponds to the Antarctic Circumpolar Current (ACC). The ACC is the

current that runs clockwise around Antarctica, and is mainly forced at the boundaries of the model, and modified by surface and tidal forcing (see Fig. 3.2). This strong correlation implies that the temporal variability in the ACC mainly controls lee wave generation in the Scotia Sea. This result providence evidence that linear theory accurately predicts lee wave generation in a partly lee wave resolving model. It remains an open question whether this will continue to apply in a model with a realistic forcing regime with higher than 700 m resolution. In addition, the variability of the lee wave signal, as for near-inertial waves, is likely to increase when smaller scales are resolved.

Chapter 5

Conclusions

5.1 Summary

We configured a high resolution, regional model to have realistic boundary, surface, and tidal forcing to investigate the internal wave field in the Scotia Sea. This thesis relied strongly on the Lagrangian filtering technique. The full domain algorithm was adapted to be more accurate, while also making it relatively more efficient. Using Lagrangian filtering, the internal wave field was separated from the non-wave component of the flow. In our model, we found that the most significant contribution to the N-scaled kinetic energy in the internal wave field is by the M_2 internal tide throughout depth in the Scotia Sea. The M_2 internal tide was found to be more temporally variable than expected ($\pm 15\%$), and cannot be assumed to be constant throughout the year. Near-inertial waves made the second largest contribution of scaled kinetic energy throughout depth. The near-inertial wave signal was found to be highly variable in time ($\pm 63\%$). Lee waves made the third largest contribution to the scaled kinetic energy near the bottom, and the fourth largest (after the $2M_2$ harmonic) at 1400 m and 100 m depth. Lee waves were found to be as variable as near-inertial waves ($\pm 63\%$).

5.2 Implications

This work suggests that the M_2 internal tide has the most kinetic energy to potentially contribute to deep ocean mixing. In our model, near-inertial waves have an order of magnitude less scaled kinetic energy than the M_2 internal tide, and thus have less potential to contribute to deep ocean mixing. Given the scaled kinetic energy in the lee wave band, our model suggests that lee waves likely make smaller contributions to deep ocean mixing in the Scotia Sea than the M_2 internal tide and near-inertial waves. This result is surprising, since various idealised simulations of the internal wave field over the last ten years suggest that lee waves make a significant contribution to deep ocean mixing. In particular, the Southern Ocean, due to its rough topography and high bottom flow speeds, is considered to be the prime location for lee wave generation.

For global circulation models, our model suggests that future parameterisations of mixing should consider the temporal variability the M_2 internal tide, as well as its temporal variability. Our model was configured for the Scotia Sea. In other regions, near-inertial waves might be a stronger signal and thus more dominant in their contribution to deep ocean mixing. However, even in the Scotia Sea, our model suggests that though the mean contribution by near-inertial waves is less, there are periods of time that can last a week

or more where near-inertial waves make second-order contributions to the kinetic energy, and thus are more likely to contribute significantly to deep ocean mixing. The strong correlation in time between lee wave generation and the deep ocean mean flow suggests that lee waves can be accurately described in terms of the temporal variations in the Antarctic Circumpolar Current.

5.3 Caveats

Higher resolution would resolve important smaller scale phenomena. By resolving a larger part of the internal wave spectrum, internal wave generation would possibly increase. Lee waves in particular are generated at smaller scales. On the other hand, by using a higher resolution, in certain regions, a bottom mixed boundary layer might form due to topographic interactions inducing turbulence. Such a bottom mixed boundary layer which would have a very small buoyancy frequency and thus would reduce internal wave generation. This work would have benefited from running the model for a longer period of time, enabling us to more robustly analyse the seasonality in the internal wave field. By running only a single year, it was difficult to distinguish model equilibration from the seasonal cycle. Much of the analysis was done across horizontal cross-sections of the ocean, which made the characterisation of certain properties of the wave field more challenging. This work would also have benefited from directly outputting the Smagorinsky viscosity (the parameterisation used for the attenuation of kinetic energy in the flow) throughout the year, which would have enabled us to investigate the connection between the scaled kinetic energy in each wave type and the dissipation of that energy.

For various purposes, it is preferable to consider the vertical energy energy flux rather than the horizontal kinetic energy. However, from computing the net vertical energy flux, there appeared to be significant reflections in the internal wave field. causing the fundamental frequency of the wave field to have little net energy flux. This motivated the choice of looking at the kinetic energy instead. By scaling the kinetic energy by N, the kinetic energy roughly scales with the total energy flux (rather than the net energy flux). This is because the vertical energy flux is related to the kinetic energy through the vertical group speed, which depends on the buoyancy frequency N, the wavenumber k, the inertial frequency f, and the frequency ω. By dividing by N, the effect of changes in the horizontal kinetic energy due to changes in the wave slope is taken into account. However, it does not take into account changes in the wavenumber. Hence, any non-linear interactions that occur between wavenumbers are not visible for analysis. Since the domain is an f-plane, the inertial frequency does not change and does not cause any difference between the energy flux and the kinetic energy. And the last variable, the frequency ω, is taken into account, since the scaled kinetic energy is analysed in the frequency.

5.4 Future work

Further work using the same model, but for a shorter period of time using a higher resolution with data being output at all depth levels would enable further analysis of many different types of important internal wave dynamics, including wave-wave interactions, mixing, dissipation, and generation. Having hourly data at all depths would allow for quantifying eddy-wave energy exchanges, and enable accurate quantification of trapping compared to reflection in the ocean. The relative amounts of trapping and reflection has

implications for deep ocean mixing, as well as for fraction of the different types of waves that reach a critical level before they reach the surface, and then contribute to mixing at that location. In our model, we found that the M_2 internal tide was not only strong near the bottom, but also near the surface. Further research should consider investigating the M_2 internal tide contribution to near-surface mixing in the Scotia Sea, and other regions in the ocean with average seafloor depths of approximately 3.5 km.

References

Alford, M. H., J. A. MacKinnon, H. L. Simmons, and J. D. Nash (2016). "Near-Inertial Internal Gravity Waves in the Ocean". In: *Annual Review of Marine Science* 8.1, pp. 95–123.

Alford, M. H., H. L. Simmons, O. B. Marques, and J. B. Girton (2019). In:

Baines, P. (1973). "The generation of internal tides by flat-bump topography". In: *Deep Sea Research and Oceanographic Abstracts* 20.2, pp. 179 –205. ISSN: 0011-7471.

Bell, T. H. (1975a). "Lee waves in stratified flows with simple harmonic time dependence". In: *Journal of Fluid Mechanics* 67.4, 705–722.

— (1975b). "Topographically generated internal waves in the open ocean". In: *Journal of Geophysical Research (1896-1977)* 80.3, pp. 320–327.

Brearley, J. A., K. L. Sheen, A. C. N. Garabato, D. A. Smeed, and S. Waterman (2013). "Eddy-Induced Modulation of Turbulent Dissipation over Rough Topography in the Southern Ocean". In: *Journal of Physical Oceanography* 43.11, pp. 2288–2308.

Cox, C. and H. Sandstrom (1962). "Coupling of internal and surface waves in water of variable depth". In: *Journal of the Oceanographic Society of Japan (20th Anniversary Volume)* 18, pp. 499–513.

Danioux, E., P. Klein, M. W. Hecht, N. Komori, G. Roullet, and S. Le Gentil (2011). "Emergence of Wind-Driven Near-Inertial Waves in the Deep Ocean Triggered by Small-Scale Eddy Vorticity Structures". In: *Journal of Physical Oceanography* 41.7, pp. 1297–1307.

D'Asaro, E. A. (1995a). "Upper-Ocean Inertial Currents Forced by a Strong Storm. Part II: Modeling". In: *Journal of Physical Oceanography* 25.11, pp. 2937–2952.

— (1995b). "Upper-Ocean Inertial Currents Forced by a Strong Storm. Part III: Interaction of Inertial Currents and Mesoscale Eddies". In: *Journal of Physical Oceanography* 25.11, pp. 2953–2958.

D'Asaro, E. A., C. C. Eriksen, M. D. Levine, C. A. paulson, P. Niiler, and P. Van Meurs (1995). "Upper-Ocean Inertial Currents Forced by a Strong Storm. Part I: Data and Comparisons with Linear Theory". In: *Journal of Physical Oceanography* 25.11, pp. 2909–2936.

Egbert, G. D. and S. Y. Erofeeva (2002). "Efficient Inverse Modeling of Barotropic Ocean Tides". In: *Journal of Atmospheric and Oceanic Technology* 19.2, pp. 183–204.

Egbert, G. D. and R. Ray (2001). "Estimates of M2 tidal energy dissipation from TOPEX/POSEIDON altimeter data". In: *Geophysical Research Letters* 30.

ERA5 Reanalysis (2017). Boulder CO: Copernicus Climate Change Service Information.

Ferrari, R. and C. Wunsch (2009). "Ocean Circulation Kinetic Energy: Reservoirs, Sources, and Sinks". In: *Annual Review of Fluid Mechanics* 41.1, pp. 253–282.

Fu, L. L. (1981). "Observations and models of inertial waves in the deep ocean". In: *Reviews of Geophysics* 19.1, pp. 141–170.

Garrett, C. (2001). "What is the "Near-Inertial" Band and Why Is It Different from the Rest of the Internal Wave Spectrum?" In: *Journal of Physical Oceanography* 31.4, pp. 962–971.

Garrett, C. and E. Kunze (2007). "Internal Tide Generation in the Deep Ocean". In: *Annual Review of Fluid Mechanics* 39.1, pp. 57–87.

Gill, A. E. (1984). "On the Behavior of Internal Waves in the Wakes of Storms". In: *Journal of Physical Oceanography* 14.7, pp. 1129–1151.

GLORYS12V1 product (2017). European Union Copernicus Marine Service Information.

Griffiths, R. W. and G. O. Hughes (2004). "The energetics of horizontal convection". In: *Proceedings of the Fifteenth Australian Fluid Mechanics Conference.*

Hughes, G. O., A. M. Hogg, and R. W. Griffiths (2009). "Available potential energy and irreversible mixing in the meridional overturning circulation". In: *J. Phys. Oceanogr.* 39, pp. 3130–3146.

Kunze, E. (1985). "Near-Inertial Wave Propagation In Geostrophic Shear". In: *Journal of Physical Oceanography* 15, pp. 544–565.

MacKinnon, J. A., Z. Zhao, C. B. Whalen, A. F. Waterhouse, D. S. Trossman, O. M. Sun, L. C. St. Laurent, H. L. Simmons, K. Polzin, R. Pinkel, A. Pickering, N. J. Norton, J. D. Nash, R. Musgrave, L. M. Merchant, A. V. Melet, B. Mater, S. Legg, W. G. Large, E. Kunze, J. M. Klymak, M. Jochum, S. R. Jayne, R. W. Hallberg, S. M. Griffies, S. Diggs, G. Danabasoglu, E. P. Chassignet, M. C. Buijsman, F. O. Bryan, B. P. Briegleb, A. Barna, B. K. Arbic, J. K. Ansong, and M. H. Alford (2017). "Climate Process Team on Internal Wave Driven Ocean Mixing". In: *Bulletin of the American Meteorological Society* 98.11, pp. 2429–2454.

Mashayek, A., R. Ferrari, S. Merrifield, J. Ledwell, L. St.Laurent, and A. Garabato (2017). "Topographic enhancement of vertical turbulent mixing in the Southern Ocean". In: *Nature Communications* 8, p. 14197.

Melet, A., S. Legg, and R. Hallberg (2016). "Climatic Impacts of Parameterized Local and Remote Tidal Mixing". In: *Journal of Climate* 29.10, pp. 3473–3500.

Mork, M. (1968). "On the formation of internal waves caused by tidal flow over a bottom irregularity". In: *Geophysical Institute, University of Bergen.*

Munk, W. H. (1966). "Abyssal recipes". In: *Deep Sea Research and Oceanographic Abstracts* 13.4, pp. 707 –730. ISSN: 0011-7471.

Munk, W. H. and C. Wunsch (1998). "Abyssal recipes II: energetics of tidal and wind mixing". In: *Deep Sea Research Part I: Oceanographic Research Papers* 45.12, pp. 1977 –2010. ISSN: 0967-0637.

Nagai, T., A. Tandon, E. Kunze, and A. Mahadevan (2015). "Spontaneous Generation of Near-Inertial Waves by the Kuroshio Front". In: *Journal of Physical Oceanography* 45.9, pp. 2381–2406.

Nansen, F. (1902). "Oceanography of the North Pole Basin: Norwegian North Polar Expedition, 1893-1896". In: *Scientific Results* 3 (9), pp. 1–427.

Nikurashin, M. and R. Ferrari (2010). "Radiation and Dissipation of Internal Waves Generated by Geostrophic Motions Impinging on Small-Scale Topography: Theory". In: *Journal of Physical Oceanography* 40.5, pp. 1055–1074.

— (2011). "Global energy conversion rate from geostrophic flows into internal lee waves in the deep ocean". In: *Geophysical Research Letters* 38.8.

Nikurashin, M., G. K. Vallis, and A. Adcroft (2013). "Routes to energy dissipation for geostrophic flows in the Southern Ocean". In: *Nature Geoscience* 6.5153, pp. 48–51.

Petterson, O. (1908). "Stromstudier vid ostersjonsportar". In: *Svenska Hydrografisk-Biologiska kommissionen* 3, pp. 13–37.

Rath, W., R. Greatbatch, and X. Zhai (2014). "On the spatial and temporal distribution of near-inertial energy in the Southern Ocean". In: *Journal of Geophysical Research: Oceans* 119.

Rayson, M., G. Ivey, N. Jones, M. Meuleners, and G. Wake (2011). "Internal tide dynamics in a topographically complex region: Browse Basin, Australian North West Shelf". In: *Journal of Geophysical Research* 116.

Scott, R. B., J. A. Goff, A. C. Naveira Garabato, and A. J. G. Nurser (2011). "Global rate and spectral characteristics of internal gravity wave generation by geostrophic flow over topography". In: *Journal of Geophysical Research: Oceans* 116.C9.

Shakespeare, C. J. (2019). "Spontaneous generation of internal waves". In: *Physics Today* 72.6, p. 34.

— (under review). "Near-Inertial Wave Propagation In Geostrophic Shear". In:

Shakespeare, C. J. and A. M. Hogg (2012). "An Analytical Model of the Response of the Meridional Overturning Circulation to Changes in Wind and Buoyancy Forcing". In: *Journal of Physical Oceanography* 42.8, pp. 1270–1287.

— (2017). "The viscous lee wave problem and its implications for ocean modelling". In: *Ocean Modelling* 113, pp. 22 –29. ISSN: 1463-5003.

Shakespeare, C. J. and J. Taylor (2015). "The spontaneous generation of inertia?gravity waves during frontogenesis forced by large strain: numerical solutions". In: *Journal of Fluid Mechanics* 772, 508?534.

Waterman, S., A. C. Naveira Garabato, and K. L. Polzin (2013). "Internal Waves and Turbulence in the Antarctic Circumpolar Current". In: *Journal of Physical Oceanography* 43.2, pp. 259–282.

Webb, D. J. and N. Suginohara (2001). "Vertical mixing in the ocean". In: *Nature* 409, p. 37.

Whitt, D. B. and L. N. Thomas (2015). "Resonant Generation and Energetics of Wind-Forced Near-Inertial Motions in a Geostrophic Flow". In: *Journal of Physical Oceanography* 45.1, pp. 181–208.

Wunsch, C. and R. Ferrari (2004). "Vertical mixing, energy, and the general circulation of the oceans". In: *Annual Review of Fluid Mechanics* 36.1, pp. 281–314.

Yang, L., M. Nikurashin, A. M. Hogg, and B. M. Sloyan (2018). "Energy Loss from Transient Eddies due to Lee Wave Generation in the Southern Ocean". In: *Journal of Physical Oceanography* 48.12, pp. 2867–2885.

Zeilon, N. (1912). "On tidal boundary-waves and related hydrodynamical problems". In: *Kungliga Svenska Vetenskapsakademiens Handlingar Ny foljd* 47.4, pp. 1–46.